



Performance and stability of a critical raw materials-free anion exchange membrane electrolysis cell

S. Campagna Zignani, M. Lo Faro, A. Carbone, C. Italiano, S. Trocino, G. Monforte, A.S. Aricò*

CNR-ITAE Istituto di Tecnologie Avanzate per l'Energia "Nicola Giordano", Consiglio Nazionale delle Ricerche, Via Salita S. Lucia sopra Contesse 5, 98126 Messina, Italy

ARTICLE INFO

Keywords:

Anion exchange membrane water electrolysis
Critical raw materials free electrocatalysts
Supported NiMo alloy
Unsupported NiFe-oxide electrocatalyst
Hydrogen

ABSTRACT

A water electrolysis cell based on anion exchange membrane (AEM) and critical raw materials-free (CRM-free) electrocatalysts was developed. A NiFe-oxide electrocatalyst was used at the anode whereas a series of metallic electrocatalysts were investigated for the cathode, such as Ni, NiCu, NiMo, NiMo/KB. These were compared to a benchmark Pt/C cathode. CRMs-free anode and cathode catalysts were synthesized with a crystallite size of about 10 nm. The effect of recirculation through the cell of a diluted KOH solution was investigated. A concentration of 0.5–1 M KOH appeared necessary to achieve suitable performance at high current density. amongst the CRM-free cathodes, the NiMo/KB catalyst showed the best performance in the AEM electrolysis cell achieving a current density of 1 A cm^{-2} at about 1.7–1.8 V/cell when it was used in combination with a NiFe-oxide anode and a 50 μm thick Fumatech FAA-3-50® hydrocarbon membrane. Durability tests showed an initial decrease of cell voltage with time during 2000 h operation at 1 A cm^{-2} until reaching a steady state performance with an energy efficiency close to 80%. An increase of reversible losses during start-up and shutdown cycles was observed. Appropriate stability was observed during cycled operation between 0.2 and 1 A cm^{-2} ; however, the voltage efficiency was slightly lower than in steady-state operation due to the occurrence of reversible losses during the cycles. Post operation analysis of electrocatalysts allowed getting a better comprehension of the phenomena occurring during the 2000 h durability test.

1. Introduction

Alkaline liquid-electrolyte water electrolysis (AWE) is currently one of the least costly technologies for water splitting from renewable power sources [1,2]. This is a mature technology for hydrogen production up to a multi-megawatt range and it represents one of the most used electrolytic technologies at a commercial level [3]. Among the different electrolysis technologies, alkaline systems are currently characterised by a lower cost of the raw materials [4]. The alkaline electrolysis stack is comparatively cheaper than other competitive technologies with low cost diaphragm separators, non-precious metals as electro-catalysts for hydrogen and oxygen evolution reactions and steel bipolar plates [5]. However, a significant disadvantage in these systems is the use of a corrosive alkaline liquid electrolyte at high concentrations, e.g. 10 M KOH [1,2,5]. This makes the electrolyte management and recirculation difficult as the concentrated KOH may easily react with carbon dioxide from the air. However, major issues of alkaline electrolyzers are a relatively low current density and operating pressure [3]. In particular, the

diaphragm does not completely prevent the produced gases from cross diffusion, which lowers coulombic efficiency. Hydrogen diffusion to the oxygen evolution chamber must be avoided to preserve the efficiency, as well as the safety of the system.

A technology competitive to AWE is the proton exchange membrane water electrolysis (PEMWE) [6]. This technology has been developed in the last decade and it is based on a proton exchange membrane separator [7]. It shows several advantages over conventional alkaline liquid electrolyte electrolysis, including significantly higher current density and hydrogen output pressure, enhanced hydrogen purity and better dynamic behaviour both in terms of fast response and load range [8]. The solid polymer membrane electrolyte in PEM electrolysis allows for a shorter ionic path between the electrodes than in the alkaline electrolyzers. The low gas crossover rate of the polymer electrolyte membrane (yielding higher hydrogen purity), allows the PEM electrolyser to safely work under a wide load range with consequent technical and economic benefits [8]. As well known, protons are characterised by higher mobility than hydroxide ions. This corresponds to enhanced

* Corresponding author.

E-mail address: arico@itae.cnr.it (A.S. Aricò).

conductivity and lower ohmic losses for a similar thickness of the electrolyte separator. However, the total ionic conductivity is the result of both concentration and mobility of conducting species. The lower mobility of hydroxide ions compared to protons is compensated in alkaline systems by using high concentration of KOH liquid electrolyte (~ 10 M KOH) [1,2,9].

Despite the specific advantages, several drawbacks still limit a large-scale deployment of PEM electrolysis technology. The acidic environment provided by the proton exchange membrane and ionomer is highly corrosive and it requires the use of rare and expensive materials. Only few materials can be selected for this harsh environment. These include noble metal catalysts in particular Ir, Pt, and Ru, and expensive Ti-based diffusion media, current collectors and bipolar plates [6–8]. Thus, a large-scale deployment of PEM electrolyzers raises significant concerns about the availability and cost of these precious raw materials. It is pointed out that beside platinum group metals (PGMs), also titanium has been included in the critical raw materials list of the EU released in 2020 [10].

Anion exchange membrane electrolysis offers a solution to several drawbacks affecting alkaline and PEM electrolysis systems [11–15]. A thin polymer electrolyte membrane separator is used as in the PEM technology with a zero-gap cell configuration [16]. The anionic polymer electrolyte allows the exchange of hydroxide ions thus creating an alkaline environment similarly to AWE [14]. An increase of current density from the present state of the art (0.5 A cm^{-2}) of liquid alkaline systems to more than 1 A cm^{-2} in AEM technology [1–3], whilst maintaining the cell voltage in a safe and efficient region ($E_{\text{Cell}} < 2 \text{ V}$) together with the exclusive use of non-critical raw materials, may contribute enormously in reducing the capital costs. The hydrogen production rate is directly related to the current density according to the Faraday law; thus, a twice-fold increase in current density compared to AWE will proportionally halve the stack costs and have a great impact on the reduction of the system costs. Moreover, AEM membranes are characterised by lower gas permeation compared to PEM systems for membrane separators of similar thickness [14–17]. Hydrogen crossover lowers the Faradaic efficiency of the electrolysis system and causes concerns in terms of safe operation. Reducing the gas crossover by using thick diaphragms in AWE, like Zirfon®, has limited the achievement of high current densities at reasonable voltage efficiencies for the cost-effective liquid alkaline technology [1,9]. Thus, the use of a thin anion exchange membrane and ionomer dispersion in the catalytic layer for enhanced catalyst-electrolyte interface allows overcoming such gaps [18]. Thus, the AEM system may effectively combine the advantages of both proton exchange membrane and liquid electrolyte alkaline technologies allowing the scalable production of low-cost hydrogen from renewable sources. The high operating internal pH of the anion exchange membrane and ionomer dispersions allows for the use of cheap and CRM-free catalysts, diffusion layers and stack plates while providing an efficient management of the gas crossover.

At the present, there are several available anion exchange membranes (Fumatech Fumasep FAA3®, Tokuyama A201®, Ionomr Aemion™, Dioxide materials Sustainion®, Hydrolite®, Orion Polymer® [19] that in principle could be utilised for AEM application [20,21]. The selection of proper cations and high ion exchange capacity can impart high ionic conductivity to the AEM membranes while the polymer backbone is a critical component to ensure chemical and mechanical stability. Ammonium-based cations appear to provide the membrane with a proper conductivity and can be used as an ionomer in the catalytic electrode layers. Amongst the most performing AEM membranes, Tokuyama A201®, Ionomr Aemion®, Hydrolite® and imidazolium-functionalized anionic polymers (e.g. Sustainion®) have shown good performance and encouraging stability [19–21]. Fumatech Fumasep FAA3® membrane also appears one of the cheapest and robust AEM polymers providing an optimal trade-off between cost and performance [16]. DABCO-crosslinked materials may enhance the AEM stability compared to conventional poly(styrene) and poly

(sulfone)-based hydrocarbon anion exchange membranes, especially when alkyl spacers are introduced between the aromatic rings and quaternary ammonium cations in poly(styrene)-based resins [20]. The spacers between the aromatic ring and the cationic group increase the alkaline stability of the materials compared to benzyl-tethered cations to styrene [20].

Regarding electrocatalysts for AEM applications, these are similar to those used in alkaline electrolyzers and are essentially based on Ni and Co materials [13,14,16,22]. Ni nanostructures with high surface area are used at the cathode [23]. Ni is known to have suitable adsorption energy for hydrogen species in the alkaline environment (H_2O and OH^-). High-surface-area Raney nickel is providing proper catalytic activity in AWE systems. Amongst the various Ni-based alloy catalysts, Ni-Mo and Ni-Cu can also provide suitable activity towards HER catalysis in alkaline condition [19,24]. However, a clear understanding of their durability is not yet available.

Ni and Co oxides, such as Co_3O_4 and NiCo_2O_4 , and Ni-Fe oxides are used as anodic catalysts [25–28]. Perovskites also possess good activity for the oxygen evolution [29,30]. However, some highly performing spinel and perovskite catalysts are based on Co and/or lanthanides that are critical raw materials thus posing issues for the availability of supply and long-term application.

Regarding the present shortcomings of AEM water electrolysis, it has been documented that most AEMs suffer from poor chemical stability [31–34]. Chemical degradation of AEMs is reported to be mainly due to a nucleophilic attack on the cationic charge sites by OH^- ions [31–34]. This causes a loss of anion-exchange functional groups and thus a decrease of OH^- conductivity producing a net increase of the ohmic resistance of the device, which translates into a large increase of the ohmic drop overpotential at high current densities, and the consequent loss of electrical efficiency. Moreover, since the ionomer used in the catalyst layer is in intimate contact with the catalyst [18], a chemical or electrochemical degradation of the ionomer may cause a significant decrease of the reaction rate. Because of the modest stability of various membranes and ionomers, the first attempts reported in the literature for AEM water electrolysis systems have shown a lifetime not exceeding 1000 h [13]. Moreover, most of the durability results have been achieved with CRM-free electrocatalysts-based electrolysis cells.

Performance and cost effectiveness of an AEM-based water electrolyser can be significantly improved by developing improved nanosized CRM-free catalysts, combining these materials with robust and cheap hydrocarbon membranes and optimising the ionomer content and the structure of the catalyst layer [35–37]. The electrode material selection for AEM electrolysis is based on a delicate balance amongst the desired corrosion resistance, high conductivity, high electro-catalytic activity and low price. Moreover, it is strongly desired that AEMWE catalysts are formed by non-critical raw materials to provide economic and long-term sustainability.

A catalyst based on a Ni structure with a high surface area can enhance the HER activity but it would still be limited by the intrinsic catalytic activity of metallic Ni. Thus, it is appropriate to modulate the chemical environment of Ni by alloying it with other metals while taking advantage of the high surface areas of Ni-based nanostructures. A nearby hetero-atom has the ability to alter surface adsorption/desorption energy on the adjacent Ni atom, and it may also provide adsorption/desorption sites for certain intermediates to facilitate the catalytic process on Ni. In particular, Mo or Cu addition to Ni catalysts can enhance the adsorption of hydroxide species [23,24,38–42]. NiMo alloys can provide superior performance and stability for hydrogen evolution than the widely used Raney Ni. The latter is less stable to current reversal on taking a cell off load [1]. NiMo prevents nickel hydride phase occurrence [43]. Most of the efforts in preparing electrodes for alkaline systems involve impregnation of metallic foams and thermal decomposition, electro-deposition, ball milling of metallic powders to form alloy particles followed by pressing to give an electrode [44]. Most of these methods provide materials which are formed by particles just smaller

than a micron. Whereas nanosized alloys [45–48] are needed to achieve current densities comparable to PEMWEs.

As above mentioned, anodic electrocatalysts consisting of nickel and cobalt with spinels and perovskite structures are active for the oxygen evolution in alkaline environment [28–49]. Beside the fact that most of these catalysts are based on Co or lanthanides (CRMs), they are also prepared with methods producing low surface area in the range of 10–20 m²/g [28]; whereas noble metal catalysts used in PEM electrolysis can reach an active surface area of 100 m²/g [50]. Moreover, high loadings in the range of a few tens of mg cm⁻² are used to boost the catalytic activity while losing in terms of ohmic drop at high current densities [1].

The aim of this work was to develop nanosized CRM-free Ni-based anode and cathode catalysts and test such systems in durability experiments in combination with a cost effective and robust anionic membrane and ionomer (Fumatech Fumasep FAA3®) [14–35] to validate the possibility of operating at proper current density (1 A cm⁻²) for water electrolysis with good durability.

For the anode, nanosized (5–10 nm) Ni-Fe catalysts such as layered double-hydroxides (LDH) i.e. (Ni_{1-x}Fe_xOOH) have been mixed, in a composite catalytic layer, with the ionomer and deposited onto Ni foams. A conductive matrix of Ni oxide is required to activate the Fe sites in NiFe oxides at lower overpotential. The formation of conductive Ni^{III}OOH phase is highly important in the case of Ni-Fe oxides to activate the Fe sites which are otherwise inaccessible to electron transfer in the nonconductive Ni^{II}(OH)₂ host lattice [51,52]. Fe substitutes of Ni atoms in the mixed oxides allow for a decrease of the average bond distances, causing a reduction of the Fe–OH/OOH bond energy giving rise to an optimal adsorbate binding energy [53–55]. To achieve such characteristics, an atomic ratio 85% at. Ni and 15% at. Fe has been selected.

With regard to the cathode, the synthesis of nano-sized metallic Ni, Ni-alloy catalysts both unsupported or dispersed on carbon support and deposited on a carbonaceous gas diffusion layer has been carried out. Incorporation of additional elements (Mo, Cu) was pursued to allow fine-tuning of the adsorption properties of the Ni cathode catalyst surface and to enhance the catalytic activity for the HER [56–59].

These approaches have allowed to strongly enhancing the current density for the hydrogen and oxygen evolution reaction at practical overpotentials owing to the large catalyst surface area and optimal interface with the ionomer and electrolyte membrane. Promising performance and stability, close to those typically achieved in PEM electrolysis, have been recorded using cheap and widely available non critical raw materials.

2. Experimental

2.1. Synthesis of cathode electrocatalysts

Different chemistries and morphologies were investigated for the cathode electrocatalyst. Contrary to PEM electrolysis, hydrogen evolution in the alkaline environment is a rate-limiting step. This requires proper tailoring of the cathode electrocatalyst in relation to the operating environment. Unsupported cathode electrocatalysts were prepared by the so called "oxalate method" [60] followed by reduction in a hydrogen stream. This approach was used for the synthesis of unsupported NiCu (50%:50% at.) and Ni. It consisted of a dissolution in deionised water of pure Ni nitrate or a mixture of Ni and Cu nitrates in a 1:1 atomic ratio. Thereafter, the solution with the metal precursors (light green colour) was added as droplets to a stirred water solution of oxalic acid and NaOH at a pH of 6.5 and kept at 60 °C for 2 h to allow formation of a metal complex between metal species and the bidentate oxalate ligands. This complex formation in an almost neutral environment avoids agglomeration of metal hydroxides as it may occur in a conventional precipitation process with concentrated alkali [60]. The next step was the decomposition of the complex to form nanosized colloidal oxides. This was achieved by increasing the temperature to

80 °C and adding H₂O₂. A solid dispersion of amorphous Ni or NiCu oxide (dark-grey colour) was formed, which rapidly precipitated. The precipitate was collected, filtered and washed to remove Na species and then calcined in air at 350 °C to remove organics and to promote formation of nanocrystalline oxide powders. Finally, the formed oxides were reduced in diluted H₂ (5% in He) at 350 °C to form metallic Ni and NiCu.

Unsupported binary NiMo catalyst, in an 80%:20% atomic ratio, was prepared by incipient wetness of the Ni-oxide precursor (obtained by the oxalate method) with (NH₄)₆Mo₇O₂₄·4H₂O (Alfa Aesar) and successive thermal reduction as in the previous cases.

Alternatively, NiMo in an 80%:20% atomic ratio, supported on Ketjenblack (KB) carbon was prepared by a conventional precipitation method [61–63]. The presence of the carbon support in this case allowed for a proper dispersion thus there was no need for synthesizing the oxalate precursor complex. The carbon support (Ketjenblack ec600j-d) was dispersed in water (18.2 MΩ cm, Milli-Q® Integral ultrapure water). Nickel nitrate hexahydrate Ni(NO₃)₂·6H₂O (97.0%, Sigma Aldrich) and (NH₄)₆Mo₇O₂₄·4H₂O were added from a previously prepared suspension. Ammonium hydroxide (NH₄OH 30%) and 1 M sodium hydroxide (NaOH, 98%, Sigma Aldrich) solutions were added dropwise until reaching pH 12 at 60 °C. The solution was stirred for 6 h. The suspension was filtered and dried at 100 °C overnight. NiMo/KB was reduced in H₂ (5% in He) atmosphere at 550 °C. In this case, the reduction temperature was increased compared to the unsupported catalyst to avoid a large amount of unreduced oxide which is typically observed with the precipitation method using an excess of alkali. The metal concentration on carbon was confirmed by TGA analysis for the supported catalyst (NiMo 40% wt. and 60% wt. carbon). A commercial 30% Pt/C benchmark cathode catalyst (HISPEC 4000 by Johnson Matthey Fuel Cell) was also investigated for comparison.

2.2. Synthesis of anode electrocatalysts

NiFe (85:15 at.%) anode electrocatalyst was prepared by a coprecipitation method using hexahydrate Ni(NO₃)₂·6H₂O (97.0%, Sigma Aldrich) and Fe(NO₃)₃·9 H₂O (98.0%, Merck) [25,51]. The precursors, in the atomic ratio (85%:15% at.) were dissolved in Milli-Q® water (18.2 MΩ ultrapure water) to form a suspension. Sodium hydroxide (NaOH, 98%, Sigma Aldrich) 0.5 M solution was added dropwise until reaching pH 9 at 60 °C. The solution was further stirred until achieving precipitation of the amorphous hydroxide. The suspension was filtered, dried and treated at 120 °C. No benchmark precious metal catalyst was used for the anode.

2.3. Physico-chemical characterisation

Physico-chemical characterisations of synthesised electrocatalysts consisted in the analysis of the structure, chemical and surface properties. The crystallographic phase and the crystallite size was investigated using a Philips X-pert 3710 X-ray diffractometer equipped with a Cu Kα radiation operating at 40 kV and 20 mA. A FEI XL 30 scanning electron microscope (SEM) equipped with energy dispersive X-ray analysis (EDX) was used to investigate the texture properties and the chemical composition whereas the morphology at a nanoscale was studied by transmission electron microscopy (TEM - FEI CM12 equipped with LaB6 filament). To complete the physico-chemical characterisation, the oxidation states of selected catalysts were studied by X-ray photoelectron spectroscopy (XPS). This was carried out using a Physical Electronics (PHI) 5800–01 spectrometer equipped with a monochromatic Al Kα X-ray source.

2.4. Anionic electrolyte

A commercial Fumasep FAA3–50® (FumaTech), membrane was used as a solid polymer electrolyte in an alkaline water electrolysis. The

ionomer was obtained from the shredded FAA3 polymer by dissolving it in an alcoholic solution at moderate temperature to form ~5 wt.% dispersion. Both membranes/ionomer were exchanged with hydroxide ions before use. More details about membrane and ionomer characteristics and exchange procedures are reported in ref [16].

2.5. Membrane electrode assembly and electrochemical studies

Preparation of the anode and cathode catalyst inks was carried out by mixing 33 wt.% of anionic ionomer (Fumasep FAA3®) and 67 wt.% electrocatalyst powder in ethanol and sonicated for 30 min [16]. Each cathode catalyst dispersion was deposited on a Sigracet 39BC substrate acting as gas diffusion layer and current collector (backing layer). A similar procedure was used for the anode catalyst dispersion; however, this was deposited onto a Ni felt backing layer (NV Bekaert SA). The total catalyst loading in the final electrodes was 2.5 mg cm⁻² for the Ni-Fe oxide anode, 1 mg cm⁻² for the benchmark precious metal-based 30% Pt/C cathode and 5 mg cm⁻² for the Ni, NiCu, NiMo, NiMo/KB cathode catalysts used in this study. Finally, a cold-assembly procedure was adopted to form the membrane-electrode assembly (MEAs) thus avoiding any undesired membrane degradation during conventional hot pressing lamination process often used in conventional PEMWE MEAs fabrication [16]. Teflon® gaskets were used for the cell sealing. The geometrical electrode area was 5 cm² for catalyst screening and durability studies; the MEAs performance was also validated in 100 cm² active area cell. Cell compression was 5 N m per each tie rod.

The MEAs were assembled in single-cell housings made of nickel plates. In all experiments, a 1 M KOH solution was supplied to the anode compartment at a flow rate of 1 ml min⁻¹ cm⁻², using a peristaltic pump, if not otherwise stated. The electrochemical investigations consisted of a galvanostatic pseudo steady-state polarisation curves (cell voltage versus current density, each experimental point in the polarisation curve was recorded after a dwell time of 2 min), galvanostatic durability tests (cell voltage vs. time) and cycled operation between 0.2 and 1 A cm⁻² (cell voltage vs. time). Polarisation experiments were carried out with an ITECH 6522C (80 V/120A) power supply system in combination with a FLUKE 8846A (240 V–6.5 Digit Precision) multimeter. Electrochemical impedance spectroscopy (EIS) analysis was carried out with a biologic potentiostat/galvanostat equipped with a 100 A booster and a frequency–response analyser module for impedance spectroscopy. The impedance measurements were carried out at several cell voltages, in a frequency range between 100 MHz–10 mHz, with an oscillation voltage of 10 mV r.m.s.

The hydrogen evolution overpotential at the benchmark Pt/C catalyst, was determined through a hydrogen pumping method experiment. A 5 cm² symmetrical cell was assembled with two Pt/C electrodes. A large flow of hydrogen (0.2 l min⁻¹ cm⁻²) was fed to an electrode compartment where also a solution of 1 M KOH was recirculated. This electrode was operated as anode to oxidise H₂. Close to the inlet, a Pt wire was immersed in the KOH solution continuously flushed with H₂ (RHE) entering into the anode compartment. This Pt wire acted as a reversible hydrogen electrode (RHE) being in contact with H₂ at the operating pH. The counter Pt/C electrode was operated as cathode to evolve hydrogen like in the conventional AEM electrolysis cell. During symmetrical cell polarisation, the cathodic potential was recorded against the non-polarised Pt wire acting as RHE and it was corrected for the IR-drop. This method allowed to determine the cathode overpotential under essentially same conditions as in the electrolysis cell. Practically, this approach allowed to bypass the issues related to the presence of evolved O₂ species which are present in the recirculating KOH at a conventional electrolysis anode which would, in principle, affect a reference electrode placed in the same solution. It is pointed out that the amount of oxygen permeated through the almost full density polymer electrolyte membrane to the cathode compartment during the conventional electrolysis process is extremely low; moreover, being the hydrogen evolution reaction much faster than the oxygen reduction

process, no mixed potential is expected at the cathode during normal operation. Thus, the hydrogen evolution overpotential determined for the Pt/C electrode in the separate hydrogen pumping experiment is essentially similar to that of the same Pt/C electrode operating during the electrolysis process.

The overpotential of the Ni-Fe oxide anode with respect to the thermoneutral potential (1.48 V [6]) was thus determined from single cell experiments using a benchmark Pt/C cathode according to the formula:

$$\eta_{\text{NiFe-anode}} = E_{\text{Cell}} - \eta_{\text{Pt-cathode}} - IR - E_{\text{th}} \quad (1)$$

where η_a is the anodic overpotential versus the thermoneutral potential for the NiFe oxide anode, E_{cell} is the overall cell potential, $\eta_{\text{Pt cathode}}$ is the overpotential of the Pt/C benchmark cathode already determined from the hydrogen pumping experiment, IR is the ohmic drop with R determined from the series cell resistance and E_{th} is the thermoneutral potential.

Since the same Ni-Fe oxide anode was always used during the assessment of the CRM-free cathode catalysts, the overpotentials of the cathodic catalysts were determined from the formula:

$$\eta_{\text{cathode}} = E_{\text{Cell}} - IR - E_{\text{th}} - \eta_{\text{NiFe-anode}} \quad (2)$$

where η_{cathode} is the overpotential of the CRM free cathode catalyst. The other terms have been defined above.

3. Results and discussion

3.1. Catalysts characterisation

CRM-free cathode catalysts consisted of unsupported Ni and NiCu prepared according to the "oxalate method", NiMo was obtained by combination of oxalate and incipient wetness methods and NiMo/KB was synthesised by an impregnation and precipitation method. The oxide/hydroxide precursors obtained by the above procedures were reduced using diluted hydrogen to form metallic species. The different compositions, preparation routes and reduction treatments were selected according to the characteristics of precursors, support and chemistry of elements involved. The objective was to achieve metallic Ni or Ni alloys with possibly similar crystallite size as determined by XRD. As discussed above, a benchmark commercial Pt/C catalyst was investigated for comparison. The average crystallite size was determined by X-ray diffraction and calculated from the broadening of the main diffraction peaks using Scherrer equation [64]. The average crystallite size is essentially related to the dimensions of crystalline domains in the catalyst particles and in the agglomerates. This can differ from the particle size determined from TEM using the atomic contrast (see below). These two parameters can give indications about the number of

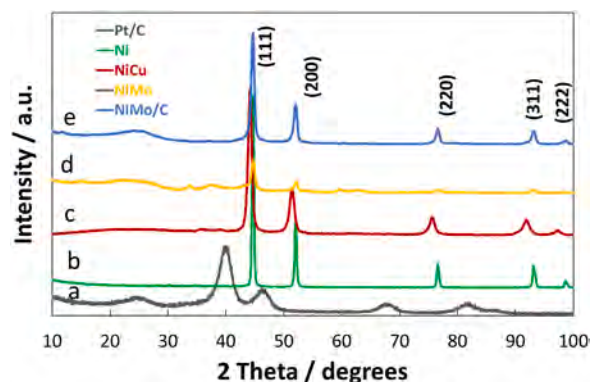


Fig. 1. X-ray diffraction patterns of Pt/C (a), Ni (b), NiCu (c), NiMo (d), and NiMo/KB (e).

active sites.

Fig. 1 shows the diffraction patterns of catalysts in their final form. Pt/C presents the typical face-centred cubic (fcc) with diffraction peaks at 40° , 46.2° , 67.9° , 81.6° and 86° Bragg angles, corresponding to (111), (200), (220), (311) and (222) reflections (JCPDS Card 04–0802). The peaks are highly broadened with a crystallite size of 2.5 nm. For the unsupported Ni (d), a cubic structure (JCPDS card 4–850) similar to Pt is observed. A crystallite size of 13 nm is determined. This is larger than the other bimetallic CRM-free catalysts. For the unsupported NiCu (c), the diffraction pattern indicates a cubic structure that is intermediate between metallic Ni (JCPDS card 4–850) and metallic Cu (JCPDS 4–836). The shift indicates the formation of an alloy with composition corresponding to the nominal one (1:1 at.) according to the Vegard's law [38–40]. The diffraction peaks are characterised by a crystallite size of 7 nm. This is smaller than pure Ni indicating that the presence of copper can mitigate particle growth during reduction while allowing achieving suitable metallic properties [24,48]. The binary unsupported NiMo shows the occurrence of metallic NiMo alloy (JCPDS card 4–850, JCPDS 4–809) and MoO_2 (JCPDS 32–681), the latter in smaller contents, with a crystallite size of 10 nm for the main NiMo species. Carbon supported NiMo/KB shows the occurrence of NiMo alloy mainly. At low Bragg angles ($20\text{--}25^\circ$), it is possible to observe the 002 reflection of graphitic carbon with a hexagonal structure as in the Pt/C catalyst. The presence of Mo oxides [58] is significantly lower in the supported NiMo catalyst compared to the unsupported one. This is essentially related to the higher reduction temperature for the supported catalyst made possible by the fact that the dispersion on carbon mitigates the particle growth, giving rise to a crystallite size of 8 nm for the carbon supported NiMo phase.

Fig. 2 shows the TEM images of carbon supported Pt/C (a) and NiMo/KB (b) as well as the unsupported Ni (c) and NiCu (d) cathode catalysts. The Pt/C catalyst shows very fine particles homogeneously dispersed over the carbon support. The NiMo/KB is characterised by significantly larger particles with spherical shape properly dispersed on carbon. The unsupported Ni catalyst shows large particles and agglomerates formed by smaller crystallites. NiCu shows lower agglomeration compared to Ni as well as smaller particles. In principle, Cu or Mo can mitigate the particles growth during the reduction process.

The diffraction pattern of the NiFeOx (Ni:Fe=5.7:1) anode catalyst shows the typical reflections of Ni hydroxide hydrate (JCPDS card n° 380,715) with rhombohedral structure [25,26,51]. This material shows both broad and narrower peaks, possibly because of the contribution of particle orientations characterised by different dimensions. An average

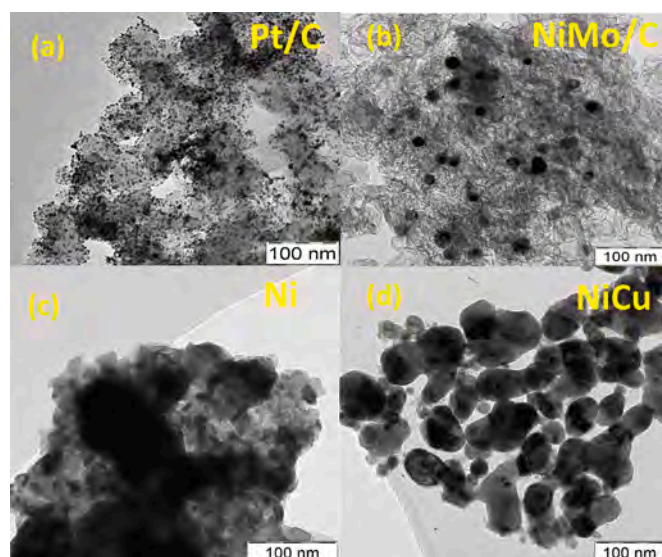


Fig. 2. TEM images of Pt/C (a), NiMo/KB (b), Ni (c) and NiCu (d) cathodes.

crystallite size of 2.7 nm was calculated using the Scherrer formula [64]. The TEM analysis of NiFe oxide deposited on a holey carbon grid (Fig. 3) shows a suitable dispersion of fine particle agglomerates with typical size of 10–20 nm. However, much smaller crystallites are also widely observed inside the agglomerates confirming the results of the crystallite size determination from XRD.

3.2. AEMWE cell characterisation

The operation scheme and specific photographs for the 100 cm² active area AEM electrolysis cell and its functional components are provided in Fig. 4. Functional components of the electrochemical cell i. e., electrodes and membranes, showed good homogeneity at different scales. H₂ evolution occurs at the cathode compartment. The CRM-free cathode catalysts selected for this process were unsupported Ni, NiCu, NiMo or NiMo/KB; whereas, oxygen evolution occurs at the anode at a NiFe-oxide catalyst to complete the electrochemical process.

All catalysts were mixed with the FAA-3 AEM ionomer [16] and deposited onto gas diffusion backing layers (carbonaceous GDL for the cathode and Ni felt for the anode) to form the electrodes. The electrodes were separated by a 50 μm thick anion exchange membrane (FAA3–50 from Fumatech) [16]. Both ionomer and membrane polymers contain ammonium functional groups allowing the exchange of hydroxide ions. The membrane avoids the recombination of the reaction products while allowing ionic percolation in the device as needed to complete the electrochemical process.

To assess the anode catalyst overpotential, a Pt/C catalyst was used at the cathode. The overpotential at this electrode was determined in a separate hydrogen pumping experiment using an RHE as discussed in the experimental part. The variation of Pt/C overpotential as function of current is shown in Fig. S1 (supplementary information). As expected, the Pt cathode was much less polarised compared to the CRM-free catalysts.

Fig. 5 show electrolysis performance comparison of CRM-free cathode catalysts and precious metal-based Pt/C as cathode at 50 °C in the presence of the same anode catalyst (NiFe-oxide) and membrane (FAA-3–50®) using 1 M KOH recirculation. It is pointed out that the catalyst loading for the cathode was 5 mg cm⁻² for all CRM-free cathode catalyst whereas it was 1 mg cm⁻² for the Pt/C and 2.5 mg cm⁻² for the NiFe oxide anode. The unsupported Ni, NiCu and NiMo showed much higher activation losses compared to Pt despite the higher catalyst loading. The initial performance increased in the sequence: unsupported NiMo < Ni < NiCu < supported NiMo/KB < Pt/C. This corresponded to a lower cell voltage at the same current density. Interestingly, the carbon supported NiMo/KB showed the best performance amongst the CRM-free catalysts despite the unsupported NiMo was the least performing cathode. This seems to be related to the relatively large content of oxide species present in the unsupported NiMo [42], as evident in the XRD diffraction pattern being the crystallite size not significantly different from the other catalysts. Whereas the NiMo/KB that was reduced at a higher temperature (550 °C vs. 350 °C) showed enhanced performance due to the relatively low content of oxide species as revealed by XRD. As above mentioned, a higher reduction temperature was selected for the supported catalyst since the metal dispersion on carbon could mitigate the particle growth. Interestingly, the NiMo/KB showed an initial performance gap of 220 mV at 1 A cm⁻² vs. the benchmark Pt/C. However, this gap reduced to 120 mV after 280 h operation (Fig. 5b).

3.3. AEMWE cell durability

Fig. 6 shows short durability tests for the electrolysis cells, based on NiCu (a) or NiMo (b) as cathode carried out in galvanostatic mode at different current densities. During such short tests, the cell based on NiCu (Fig. 6a) showed the occurrence of relevant losses in a relatively small time-window; this behaviour seemed to be independent from the current density applied to the cell. Thus, the rapid deactivation appeared

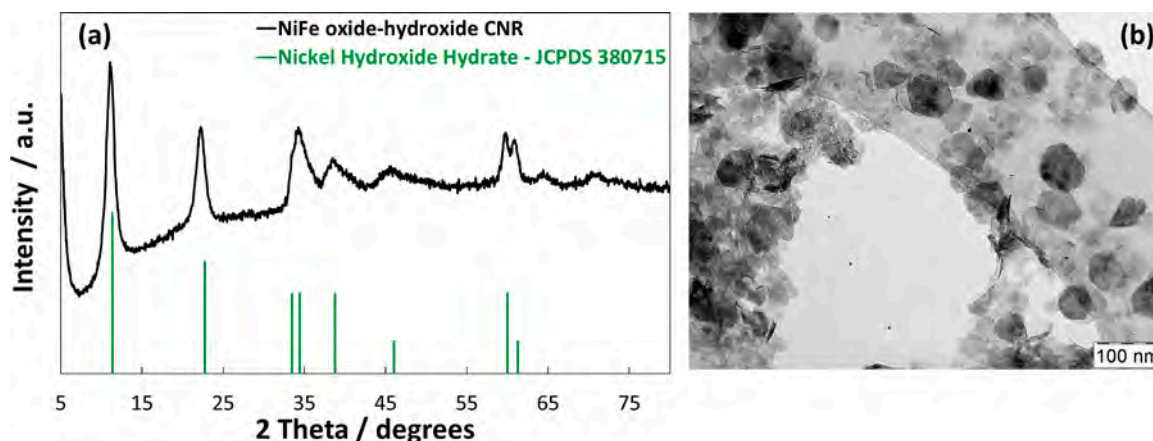


Fig. 3. Unsupported NiFe oxide: X-ray diffraction pattern (a), TEM micrograph (b).

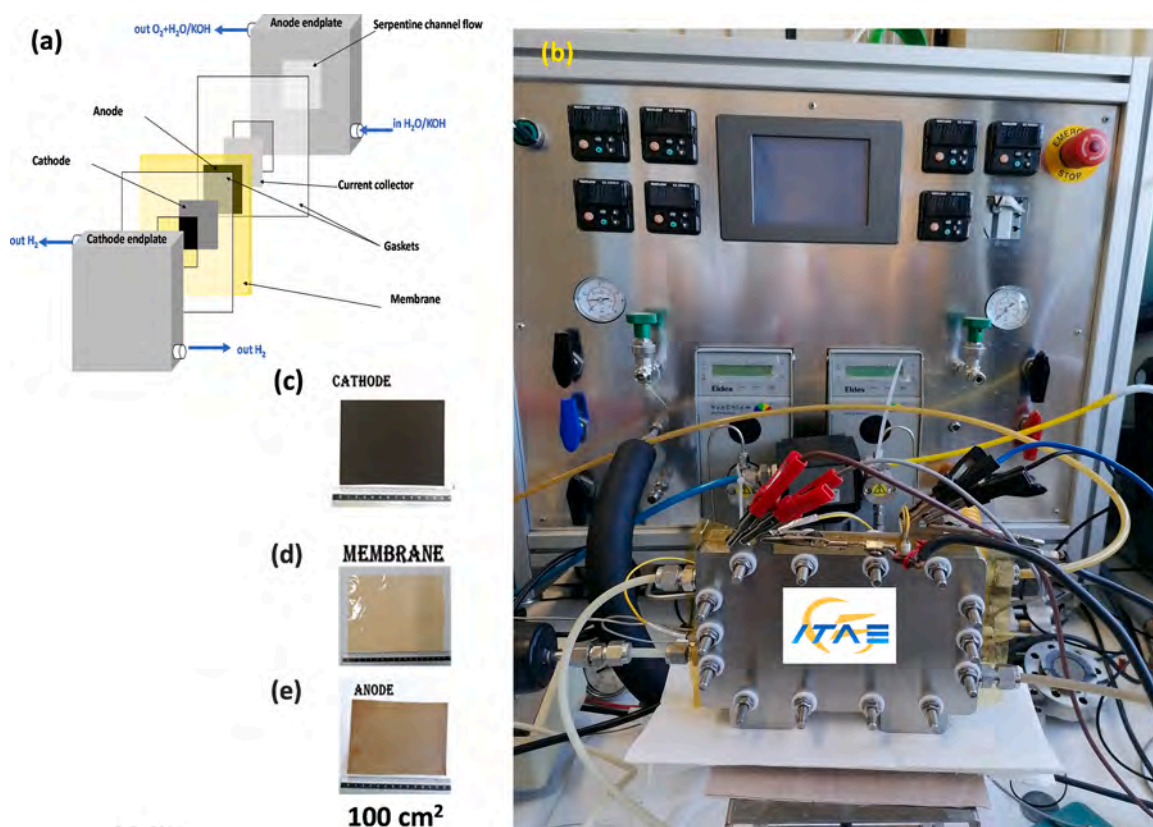


Fig. 4. (a) Scheme of a single cell unit used for the electrochemical assessment. (b) electrolysis test station equipped with 100 cm² active area cell. Cathode (c); Fumatech® membrane (d) and anode (e) for a 100 cm² active area cell.

to be caused by the simultaneous occurrence of recoverable and unrecoverable losses. Unrecoverable losses could be related to some chemical dissolution of Cu species causing ionomer and membrane poisoning. Cherevko studied the stability of Ni-metal catalysts used for hydrogen oxidation in AEM fuel cells [65]. Cu was found stable below 0.4 V vs. RHE but it could undergo to transient dissolution in the AEM environment. Degradation of Cu under cathodic operation conditions in alkaline environment is not so evident in the literature and the present evidences may be related to the specific catalyst properties and/or operating conditions. Since the membrane was relatively stable in the presence of NiFe-oxide anode and Pt/C cathode such performance decay appeared to be related to the NiCu cathode. Recoverable losses appeared instead to be related to diffusion constraints possibly due to the catalyst

agglomeration as observed in Fig. 2.

Fig. 6b shows the durability test of a cell based on NiMo as cathode carried out in galvanostatic mode at 0.5 and 0.6 A cm⁻² after conditioning at lower current density (not shown).

Contrary to NiCu, the unsupported NiMo catalyst showed a decrease of cell voltage with time when the electrolysis current passed in the cell; this decrease of cell voltage was especially relevant at high current density e.g. 0.5 and 0.6 cm⁻² (Fig. 6b). Such effect was interpreted as due to a catalyst modification during the steady-state operation such as an in situ reduction of the surface oxides. This hypothesis was confirmed by post-operation analysis where the content of Mo-oxide species appeared considerably lower after prolonged electrolysis operation (see below). As well known, metallic species on the cathode surface are

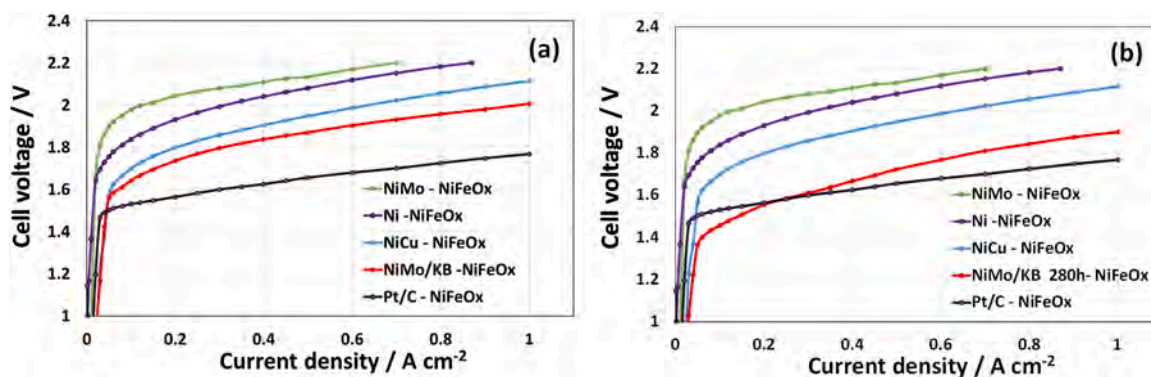


Fig. 5. Comparison of AEMWE cell polarisation curves at 50 °C based on NiMo, Ni, NiCu, NiMo/KB and Pt/C at the cathode. (a) reports the initial performance of NiMo/KB; (b) reports the performance of NiMo/KB after 280 h operation. The cell consists of FAA-3-50 membrane and NiFe-oxide anode.

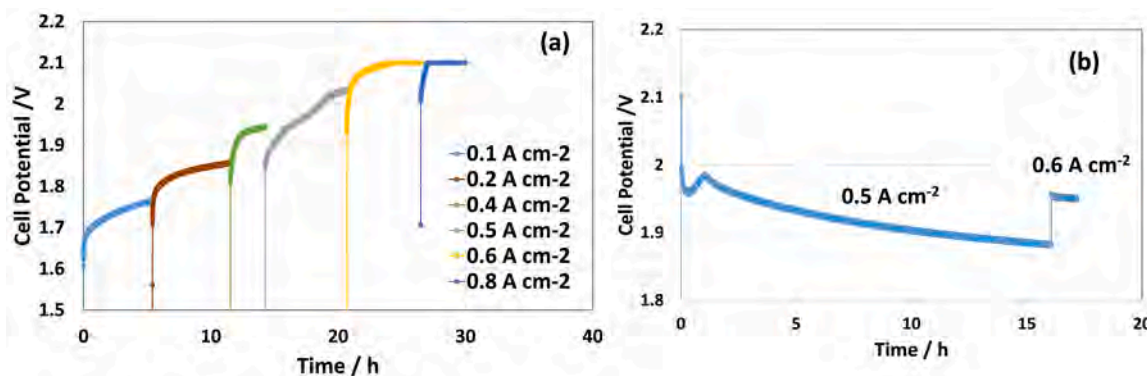


Fig. 6. Durability test carried out at 50 °C at different current densities for cells based on NiCu (a) and NiMo (b) as cathode, FAA-3 membrane and NiFe oxide as anode.

considered essential to promote the adsorption of hydrogen species [23, 38]. These results prompted us to explore catalyst reduction at higher temperature while using a carbon support to favour the dispersion of metal precursor. This avoided particles growth during the high temperature reduction treatment. The NiMo/KB that was reduced at high temperature showed promising performance (Fig. 5) already from the beginning while still having a moderate content of oxides on the surface as revealed by XRD and XPS (see below). The NiMo/KB catalyst was thus investigated in the electrolysis cell with prolonged conditioning at low current density to favour a progressive reduction of oxide species.

Fig. 7 reports the measured cell voltage during an electrolysis durability test of about 2.000 h under galvanostatic operation conditions at 1 A cm⁻² for a cell based on NiMo/KB cathode, NiFe-oxide anode and FAA-3-50 membrane. To monitor the evolution of the cell behaviour by

using electrochemical diagnostics, several start-up and shutdown cycles were carried out during the test; some of these interruptions were also needed to carry laboratory maintenance work during the 2000 h durability test. During this test, the cell voltage rapidly increased in the first hours of operation indicating the occurrence of recoverable losses (mass transfer issues); after an initial induction period (~100 h), the cell showed a continuous voltage decrease corresponding to an increase of cell efficiency. However, several reversible losses were detected upon start-up after a shutdown period. A possible explanation for the reversible losses may regard some diffusion constraints affecting the release of produced gas or some carbonation phenomena affecting the cell during the shutdown period.

It is pointed out that KOH is fed to the anode only and it reaches the cathode by a diffusion effect. Whereas the electroosmotic drag forces the

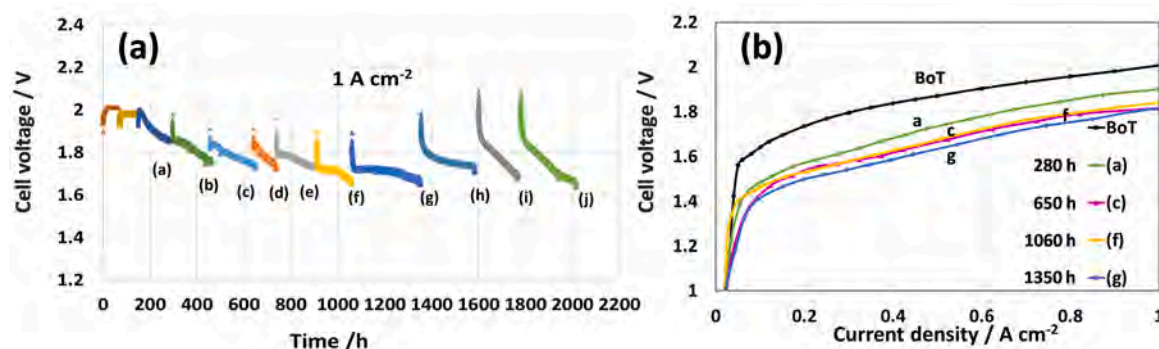


Fig. 7. (a) Durability test carried out at 50 °C at 1 A cm⁻² for the cell based on NiMo, NiFe oxide catalysts and FAA-3-50 membrane; (b) polarisation curves carried out at different operating times corresponding to beginning of test and durability test interruptions a), c) f) g) in the durability experiment.

formed hydroxide ions to migrate from the cathode to the anode according to the reaction stoichiometry [1,5]. Thus, a delicate balance between the water permeated by diffusion through the membrane and that leaving the cathode by the electroosmotic drag is the key aspect influencing the cathode wetting. Moreover, carbonation phenomena may occur. Uptake of CO_2 in the cell from the external environment may especially occur during shut-down periods. The formed carbonate species may initially poison both electrodes and membrane and could thereafter decompose during the start-up of each new electrolysis cycle releasing the adsorbed CO_2 . This may cause an initial rise of cell voltage followed by rapid decrease of cell voltage once the electrolysis process takes place.

Regarding the continuous increase of voltage efficiency versus time, under steady-state conditions, this appears related to two possible phenomena occurring within the catalytic layers: a progressive reduction of oxides on the surface of NiMo/KB and an increased uptake of hydroxides by the Ni-Fe anode. These aspects were confirmed by X-ray photoelectron spectroscopy (XPS) analysis (see below). A significant reduction of the activation losses, during prolonged operation, was evident in the polarisation curves subsequent to the beginning of test (BoT) experiment and it corroborated these hypotheses. Another, interesting aspect is regarding the change of slope at about 0.3 A cm^{-2} in the polarisation curves of Fig. 7b acquired in between steady state cycles. Such rise in cell voltage is possibly another evidence of diffusion constraints occurring in the high current density range.

Ac impedance spectra carried out at different operation times and at various cell voltages are shown in Fig. 8. These impedance spectra showed at the beginning of test, at 1.8 V, a polarisation resistance (R_p) value of 1.04 Ohm cm^2 . Successively, R_p values varied between 200 and

300 mOhm cm^2 at 1.8 V and between 150 and 200 mOhm cm^2 at 2 V (Fig. 8). Polarisation resistance was determined as a difference between low and high frequency intercepts on the real axis. The small oscillations observed for the polarisation resistance values, after the initial conditioning period, may reflect specific cell conditions including the occurrence of reversible losses. Series resistance (R_s) values were typically in the range of 150 mOhm cm^2 excluding the last period of testing where R_s values as low as 120 mOhm cm^2 were observed. The evolution of R_p and R_s is plotted versus time in Fig. 8. The rapid decrease of R_p in the first hundreds hours is well noted; thereafter, this value remains almost constant; the slight decrease of R_s is also noted. This confirms the progressive electrode activation and possibly some membrane thinning by the end of test.

Faradaic efficiency was determined by measuring the amount of dry gas produced at cathode and the gas composition. Pure hydrogen was produced at the cathode with a faradaic efficiency better than 99% at the beginning of the durability test (Fig. S2, supplementary information). Combining an average voltage efficiency of 82% ($1.48 \text{ V}/1.8 \text{ V}$) and 99% faradaic efficiency at 1 A cm^{-2} , the overall energy efficiency approximates 81%. However, the faradaic efficiency decreased to about 96% at the end of the 2000 h durability test indicating an increase of hydrogen losses with time possibly related to an increased permeation through the membrane as consequence of a membrane thinning, as it would account the decrease of series resistance by the end of the test. The hydrogen purity at the cathode remained substantially similar.

3.4. Surface characterisation and post-operation analysis

The surface composition was essentially investigated for the selected

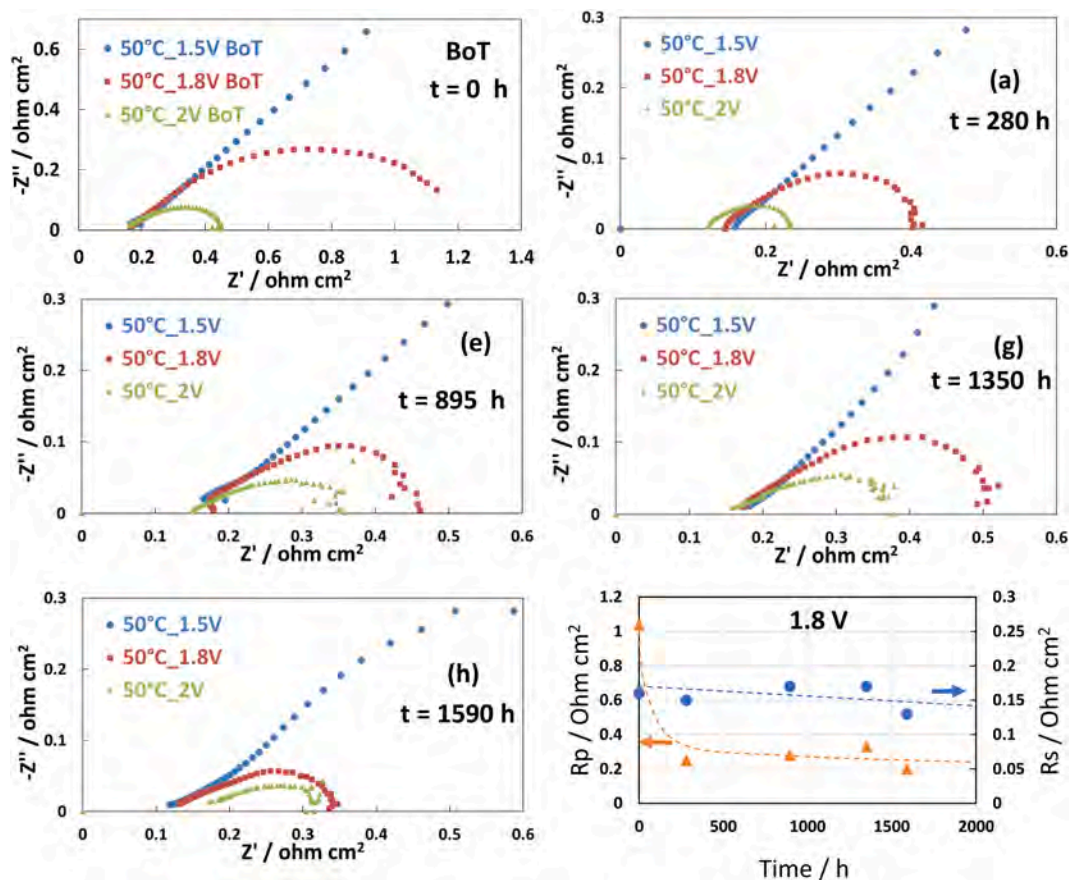


Fig. 8. Impedance spectra at different operating times corresponding to beginning of test (BoT) and specific interruptions of the durability test in Fig. 7, i.e. interruptions a), e), g), h). Frequency decreases from left to right. Evolution of the series (R_s) and polarisation (R_p) resistances with time at a cell voltage of 1.8 V (bottom, right).

CRM-free catalysts used in durability tests i.e. NiFe anode (Fig. 9) and NiMo/KB (Fig. 10). XPS analysis of the NiFe-oxide (Fig. 9) showed mainly the presence of NiO (Ni 2p_{3/2} at 854 eV), Ni(OH)₂ (Ni 2p_{3/2} at 856.6), and FeOOH (Fe 2p_{3/2} at 711 eV) [66]. The latter correlated with as a mixture of oxide and oxide-hydroxide species [67]. A small shoulder at lower B.E. (Fe 2p_{3/2} at 705 eV) in the Fe2p spectrum could be related to the occurrence of reduced Fe species [66] that should undergo to rapid oxidation during operation at high potentials in the electrolysis environment. The atomic ratio of Ni:Fe on the surface was 65%:35% at. This confirms for the catalyst surface the same chemical properties observed by XRD, which is essentially related to the bulk characteristics.

The XPS analysis of NiMo/KB (Fig. 10) showed mainly the presence of metallic Ni at 852.4 eV, Ni(OH)₂ at 855.6 eV and MoOx (Mo 3d_{3/2} Mo⁴⁺ B.E. 232.6 eV; Mo⁶⁺ B.E. 235.8 eV) [66], with an atomic Ni:Mo ratio on the surface of 78%:22% at.

It was interesting to compare the XPS analysis of the electrode surfaces before and after 2000 h operation at 1 A cm⁻². Whereas, the XRD analysis was less indicative since it included the contribution from the diffusion backing layers (not shown).

Fig. 11 shows a comparison of the survey spectra for anode (a) and cathode (b) before and after 2000 h electrolysis operation. The used anode showed a clear uptake of potassium corresponding to KOH adsorption on the surface and no relevant change in the Ni/Fe ratio. The used cathode also showed a clear uptake of potassium even if KOH was recirculated at the anode only. This confirmed the diffusion of KOH through the membrane by effect of the concentration gradient. Moreover, the carbon signal decreased drastically in the used cathode. This would indicate that, before use, a carbon film covered the active phase whereas this carbon over layer probably decomposed during operation allowing for a better exposure of NiMo particles to the reaction interface probably accounting for the increased performance with time. The Mo signal decreased dramatically after operation clearly indicating a partial dissolution of this element. According to the study of Cherevko et al [65], Mo suffers from intense dissolution in AEM fuel cells due to its thermodynamic instability. These phenomena should be less exacerbated under cathodic operation; however, unstable Mo species seem to undergo dissolution also under these conditions.

Fig. 12 shows a detailed comparison of the Ni and Fe XPS signals before and after operation. Similar electronic states were observed in the fresh and used sample corresponding to the species discussed above. In the used sample, a small shoulder was observed at 857.5 eV in the Ni 2p_{3/2} signal (Fig. 12a) that could be attributed to the presence of Ni³⁺ species [68] possibly related to the operation at high potentials. The Fe2p_{3/2} (Fig. 12b) showed a shift of 1–2 eV to higher B.E. in the used sample compared to the fresh one indicating, also in this case, a higher oxidation state associated to the high operating potential [27].

Fig. 13 shows the comparison of the Ni and Mo XPS signals before and after operation. The main Ni2p_{3/2} peak appeared shifted to negative B.E. after operation indicating a lower oxidation state on the surface but still in the range associated to Ni hydroxides (Fig. 13a) partially

overlapping to the metallic Ni contribution at 852.7 eV. The Mo amount decreased after operation and a large reduction of the MoO₃ content at 232.3 eV occurred in favour of MoO₂ at 231.6 eV (Fig. 13b). However, the small contribution of metallic Mo at B.E. 228 eV in the fresh sample was no more observed in the used sample.

Reduction of high oxidation state Ni and Mo species during electrolysis operation, removal of the carbon over layer covering the active NiMo species and uptake of KOH are distinctive chemical features that could explain the reduction of polarisation resistance in the first period of operation. However, morphological changes in the catalysts may also be relevant in determining the variation of cell performance.

Fig. 14 shows the TEM images and related EDX spectra of the fresh NiMo/KB cathode before and after 2000 h operation. After prolonged operation, the particles were still homogeneously dispersed over the carbon support even if the size of the agglomerates appeared larger than in the fresh sample. However, some of these agglomerates appeared fragmented in the used sample showing clusters consisting of much smaller particles (highlighted in Fig. 14d–e). This could have occurred due to the reduction of oxides or to some dissolution of Mo during operation. Both phenomena gave rise to a porous structure consisting of small particles in large agglomerates. These small crystallites may also be responsible for the enhanced activity during electrolysis operation.

Fig. 15 indicates essentially an increased agglomeration for the unsupported NiFe-oxide anode after operation. However, no relevant particle growth was observed after operation.

According to the post operation analysis, it is derived that chemical and morphological changes occurring at the cathode during the electrolysis process could have determined the enhanced voltage efficiency of the system. On the other hand, an increased agglomeration of catalyst particles and possibly carbonation phenomena may be responsible for the increased diffusion constraints related to the observed reversible losses.

3.5. Electrode overpotentials and Tafel analysis

Cathode overpotentials for selected catalysts such as unsupported NiCu and NiMo/KB (after 280 h operation) are shown in Fig. 16. The cathode overpotentials were relatively higher for NiCu compared to NiMo/KB in the same range of current densities. In general, overpotentials at CRM-free catalysts were significantly larger than Pt/C (see Fig S1). An activation step for the cathodic process is generally related to the formation of hydrogen bonds on the surface (adsorption step). This is a slower process on Ni compared to Pt. However, the significantly higher overpotential at CRM-free cathode catalysts may be also related to their larger crystallite size compared to Pt (7–10 nm vs. 2.5 nm) corresponding to a lower active surface area.

The larger overpotential for hydrogen evolution observed at NiCu compared to NiMo/KB could be related to a lower intrinsic activity of NiCu and/or to the better dispersion shown by the supported NiMo catalyst. The crystallite size was essentially similar in the two catalysts

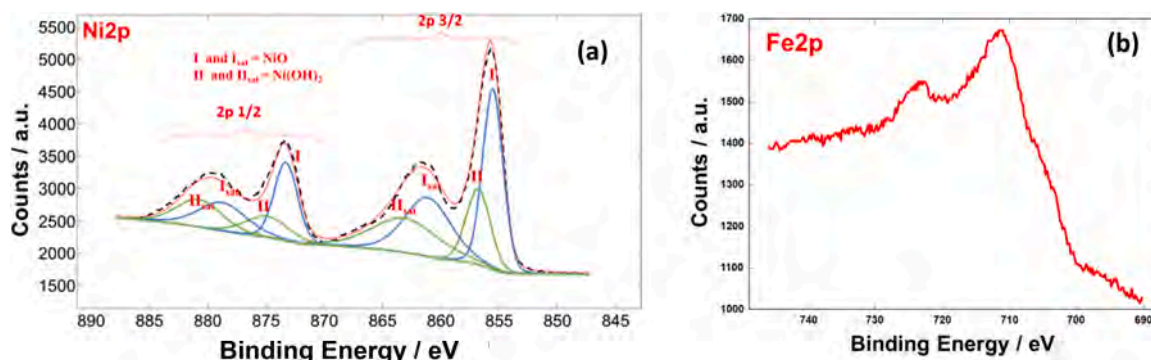


Fig. 9. XPS analysis of NiFe oxide-hydroxide before sputtering with peak deconvolution.

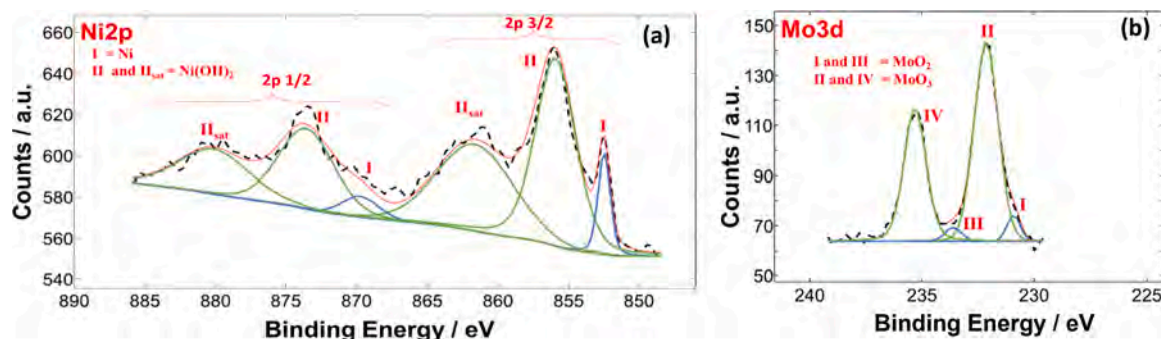


Fig. 10. XPS analysis of NiMo cathode catalysts.

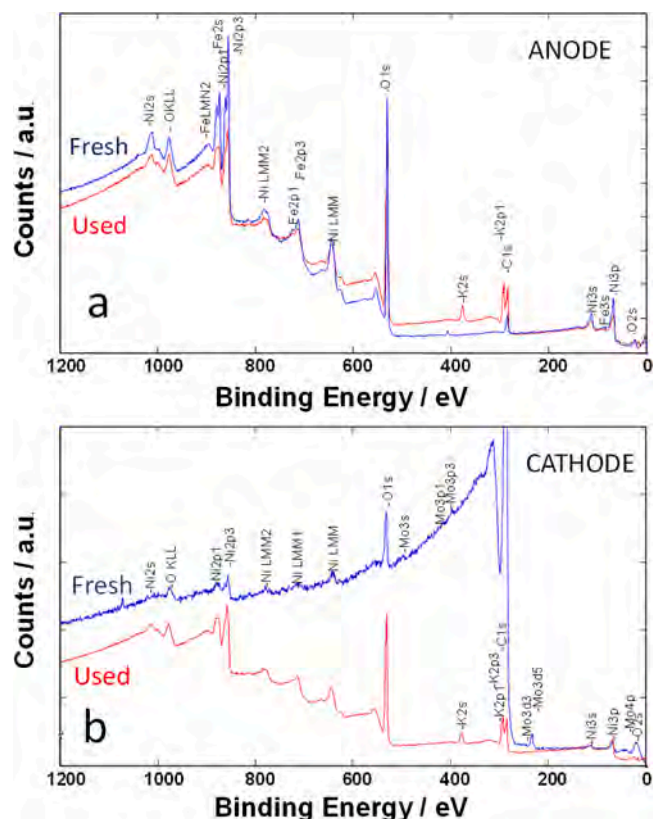


Fig. 11. Comparison of XPS survey spectra after for anode (a) and cathode (b) before and after 2000 h electrolysis operation.

but the high degree of agglomeration of NiCu as observed by TEM analysis could have a negative impact on the catalytic performance. The particle size observed from TEM was larger for NiCu corresponding to a lower active surface area. Interestingly, the Tafel slope was lower for NiCu compared to NiMo/KB. A Tafel slope of 137 mV/dec for H₂ evolution at NiCu could indicate a one-electron transfer [69–71] as rate determining step (r.d.s.). This is relatively close to the Tafel slope typically observed for a Volmer process (120 mV/dec) involving electroadsorption of H-species on a metallic surface as the rate determining step [24]. The observed Tafel slope is similar to that reported in the literature for NiCu alloys [24]. The Tafel slope decreased significantly for this catalyst at high current densities. As discussed above, the main issue associated to NiCu was essentially the poor durability with time despite the promising initial electrokinetic properties. Dispersion of NiCu on carbon could eventually enhance the activity but not overcome the drawback related to durability. For such reason, no attempts were made in this regard.

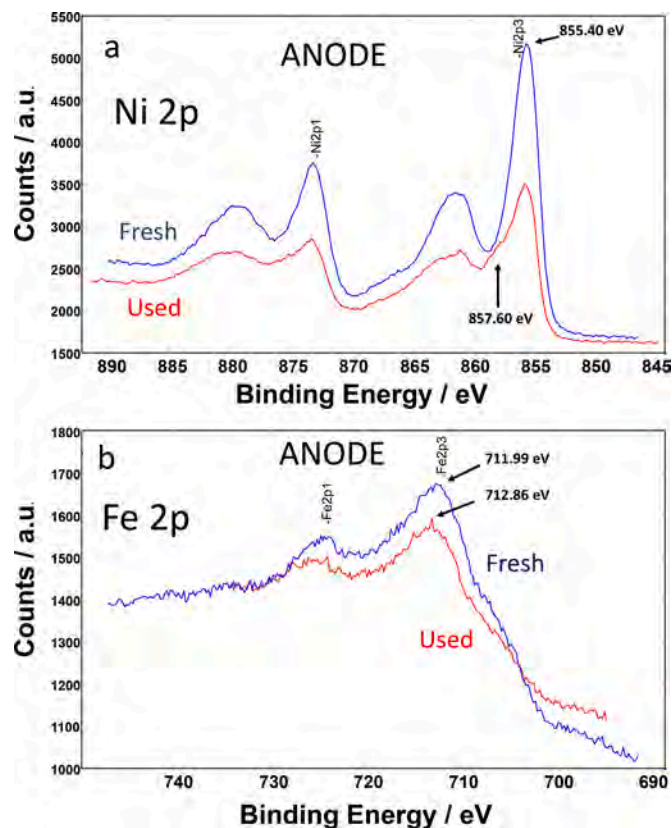


Fig. 12. Comparison of XPS spectra for the Ni 2p (a) and Fe 2p (b) signals in the anode before and after 2000 h electrolysis operation.

The Tafel slope of NiMo/KB was relatively high i.e. 230 mV/dec about. The observed value is significantly higher than that reported in the literature for a Ni-MoO₂ catalyst (120 mV/dec) [58]. This probably accounts for the occurrence of diffusion limitations causing reversible losses in the durability test with NiMo/KB [69–71]. It is not clear if such diffusion limitations may be related to the carbon support. However, this usually plays an important role in enhancing the catalyst dispersion [72]. Also in the case of NiMo/KB, the Tafel slope decreased substantially at high current density. It is observed that high Tafel slopes of about 190 mV/dec, have been reported for alternative highly efficient PGM-free catalysts-based MEAs used in AEM electrolysis [13].

Overpotentials at the NiFe-oxide anodic catalyst were similar to those recorded for the best CRM-free cathode catalysts (Fig. 16c). A Tafel slope of 116 mV/dec for O₂ evolution at the NiFe-oxide in the AEM electrolysis cell could also account for a 1e⁻ transfer mechanism as rate determining step [69–71]. This is substantially higher than that observed in half cell studies for NiFe hydroxide electrocatalysts used for

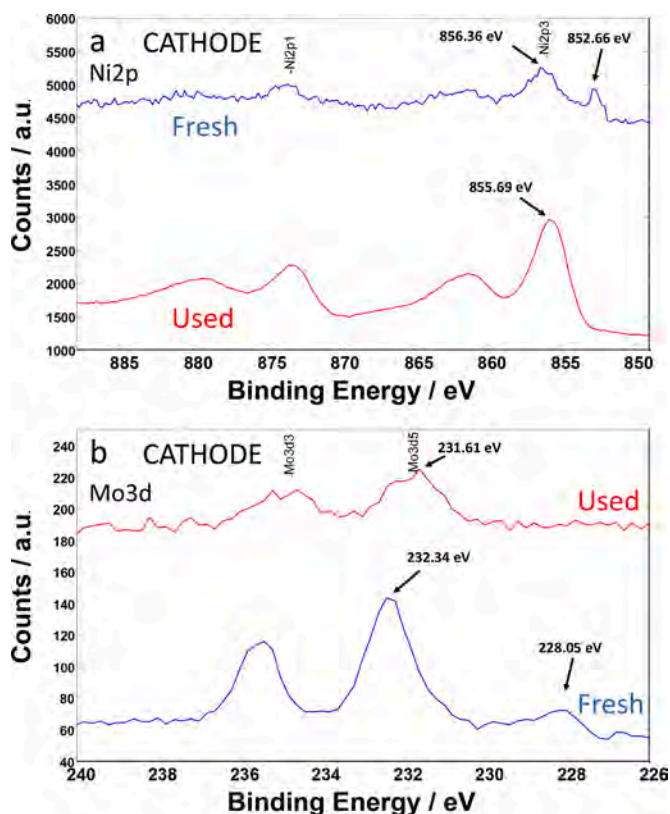


Fig. 13. Comparison of XPS spectra for the Ni2p (a) and Mo 3d (b) signals in the cathode before and after 2000 h electrolysis operation.

the oxygen evolution process (33–45 mV/dec) [49] and it can be related to the different catalyst properties and operating conditions, e.g., a higher operation current densities range. The large slope observed at increasing current densities may be also in this case indicative of mass transfer constraints.

3.6. Effect of KOH feed concentration on electrolysis performance

The performance variation as function of the concentration of the recirculating KOH solution was investigated in a 100 cm² cell (Fig. 17). These experiments were carried out using an MEA based on a NiMo/KB cathode, a FAA-3–50 membrane and a NiFe anode. This specific comparison was carried out after a short conditioning period of just 24 h. The investigated concentrations were 0.1, 0.5 and 1 M KOH and pure water. The performance achieved with pure water and 0.1 M KOH was significantly lower than what observed at high concentrations of recirculating KOH solution. Interestingly, at low current densities, operation with 0.5 M KOH provided a performance slightly better than with 1 M KOH. This would indicate that the concentration of hydroxide ions is sufficiently high at 0.5 M KOH to promote reaction kinetics while the adsorption of potassium ions on the electrocatalyst surface, as revealed by XPS analysis, could be lower than with 1 M KOH. This may have an impact on the effective number of catalytic sites on the electrode surface available for the electrochemical process. At high current densities, the better conductivity achieved with 1 M KOH provided an enhanced performance at 1 A cm⁻². The lower slope of the polarisation curve obtained with 1 M KOH in the ohmic drop controlled region suggests a positive contribution in terms of ionic conductivity by the recirculating solution which is particularly relevant at high current densities.

Impedance spectra carried out at 1.5 and 1.8 V are shown in Fig. 18. At 1.8 V, corresponding to practical current densities, the series resistance progressively increased from about 0.15 to 0.25 Ohm cm² as the KOH concentration decreased from 1 to 0.1 M. It further increased to 0.64 Ohm cm² in pure water. The polarisation resistance increased significantly for the cell fed with 0.1 M KOH (~0.7 Ohm cm²) and pure water (~2.62 Ohm cm²) compared to about 0.3 Ohm cm² registered at 0.5 M KOH concentration. These results clearly indicate that lowering the KOH concentration to 0.1 M or using pure water can cause more electrokinetic constraints than ohmic losses in the investigated potential region. By using a nickel-based microporous layer, Razmjooei, et al. achieved an AEM electrolysis performance of about 2.5 V at 0.5 A cm⁻² in pure water [73]. Whereas performance increased considerably using precious metal electrocatalysts [73]. By using precious metal electrocatalysts, such as Pt black and IrO₂, in combination with a PaperION® membrane, a promising performance of 1.9 V was recently achieved at 1 A cm⁻² by Boettcher et al. [74]. This is a further confirmation of the

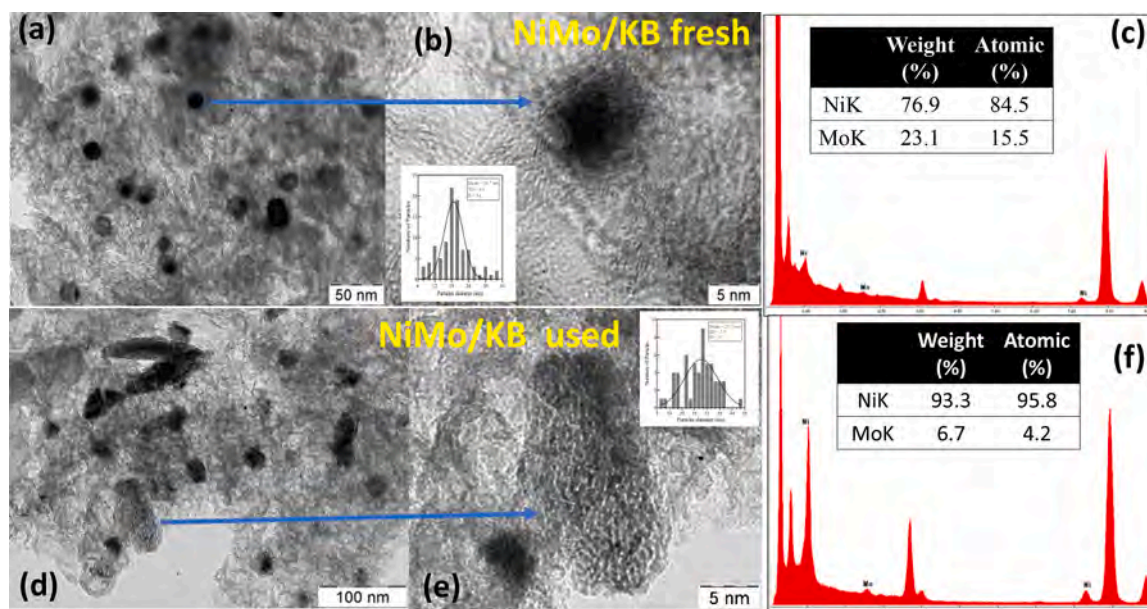


Fig. 14. TEM images of NiMo/KB fresh cathodes (a,b), EDX analysis of fresh NiMo/KB (c); TEM images of the NiMo/KB used cathodes (d,e), EDX analysis of used NiMo/KB(f). Cu, O and C signals from the sample grid and catalyst support are not labelled.

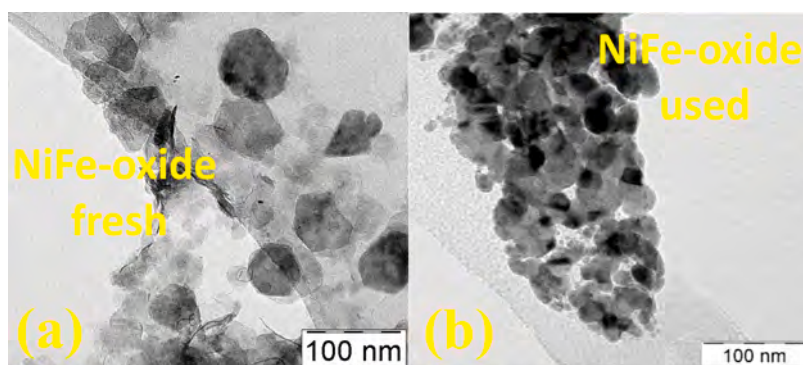


Fig. 15. TEM images of NiFe-oxide catalyst fresh (a) and after operation (b) deposited onto holey carbon grids.

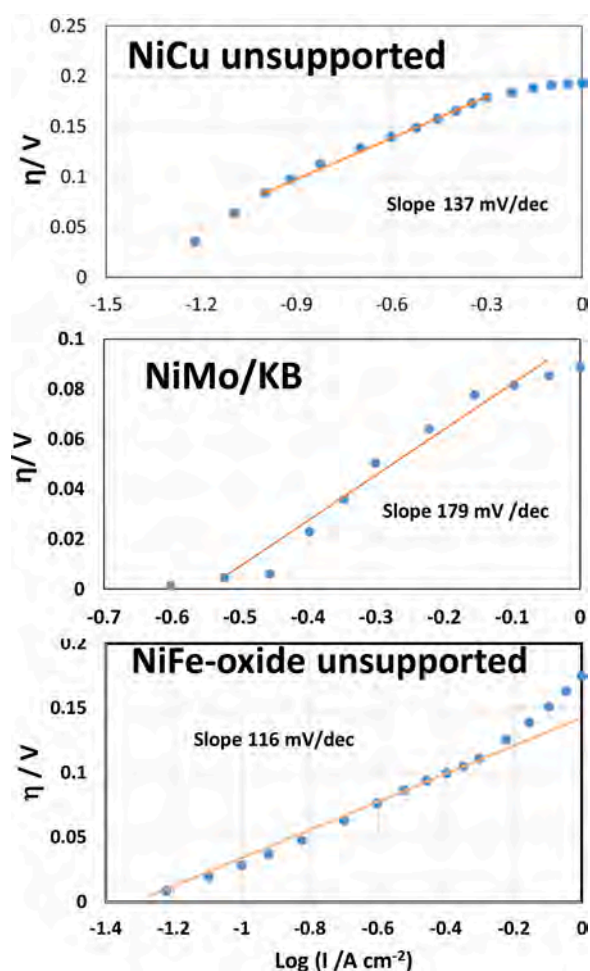


Fig. 16. Tafel plots for CRM-free cathodic and anodic electrocatalysts.

evidence that operation of AEMWE with pure water or very low concentration KOH is mainly hindered by kinetic limitations and, in the absence of precious metal materials, it requires further development of the CRM-free electrocatalysts. Unfortunately, there are not many literature reports on prolonged electrolysis operation with pure water, e.g., in the range of a thousand of hours, to understand possible membrane carbonation phenomena. On the other hand, recirculation of a moderate concentration of KOH allows using CRM-free catalysts at high voltage efficiency with a minor impact on the complexity of the electrolysis system management.

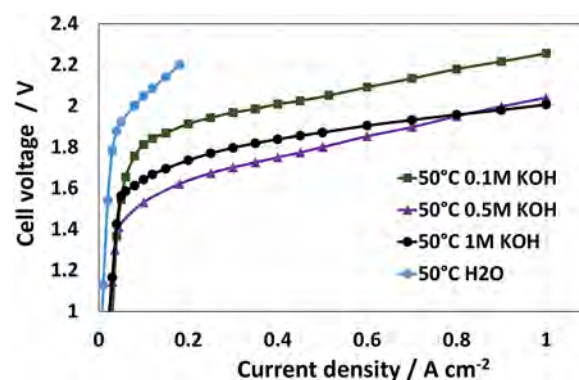


Fig. 17. Polarisation experiments in a 100 cm² electrolysis cell at different concentrations of KOH; 1 M (a), 0.5 M (b) and 0.1 M (c) and pure water (d) after 24 h cell conditioning.

4. Conclusions

This work has focused on developing CRM-free anode and cathode catalysts for stable operation at high current density and with low overpotential in an anion exchange membrane-based electrolysis cell. Nanosized NiFe-oxide for the anode and Ni or Ni-alloys for cathode were synthesized and investigated in terms of structural, morphology and surface properties. Their performance and stability were assessed in electrolysis cells in the presence of anion exchange membrane and ionomer. A commercially available Fumatech membrane FAA3-50® was chosen for this study. NiCu showed promising performance but also rapid degradation. NiMo dispersed on carbon showed the best performance amongst the CRM-free anodes. Achievement of optimal performance, required a cell conditioning of about 100 h. Proper voltage efficiency was achieved in a 2000 h durability test. High performances of 1 A cm⁻² at 1–7 –1.8 V during a steady-state stability test with 1 M KOH recirculation through the cell were achieved even if an increase of reversible losses was recorded by the end of the test. Post operation analysis showed reduction of high oxidation state Ni and Mo species in the NiMo/KB catalyst; moreover, some dissolution of Mo from the cathode was observed during prolonged operation. However, both phenomena give rise to the formation of nanosized crystallites. These chemical and morphological changes occurring at the cathode could have determined the enhanced voltage efficiency of the cell during the durability test. On the other hand, an increased agglomeration of catalyst particles, and possible carbonation phenomena may have caused the increased diffusion constraints with time and the occurrence of reversible losses. Tafel slopes were in most cases indicative of a one-electron transfer rate-determining step. The developed materials showed proper performance also in the case of diluted KOH concentration in particular in the presence of a 0.5 M KOH solution recirculated through

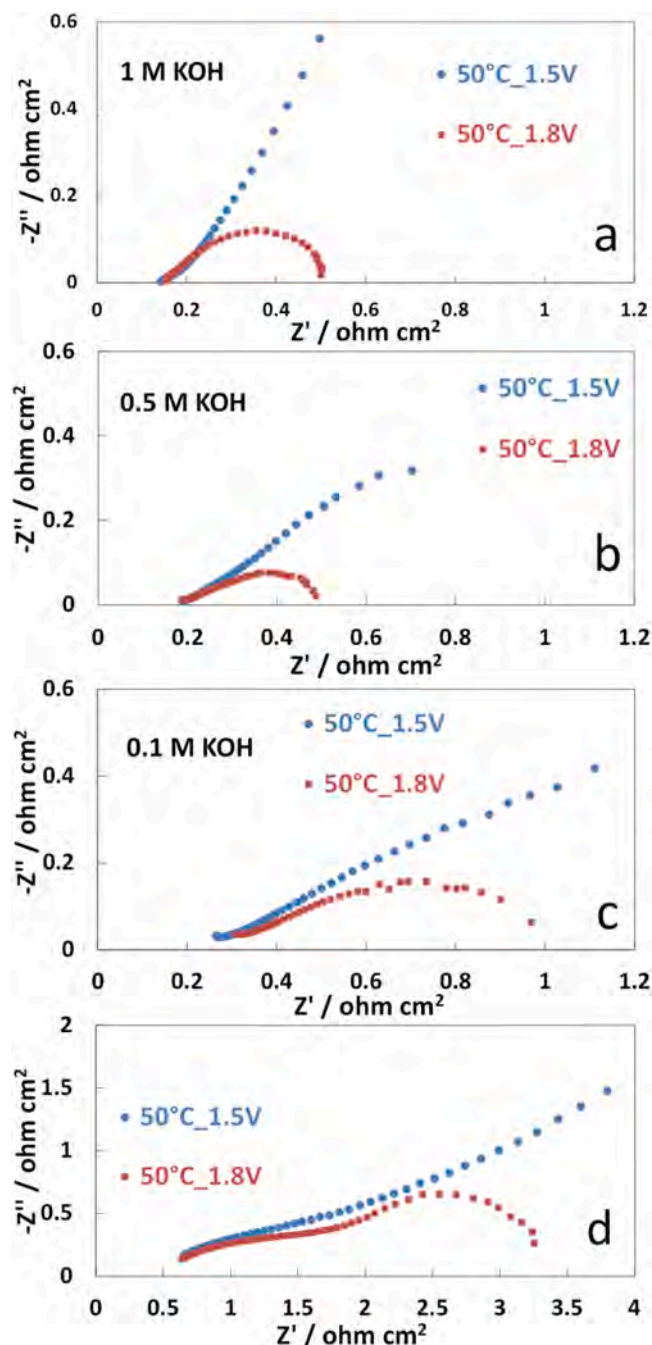


Fig. 18. Impedance tests in a 100 cm² electrolysis cell at different concentrations of KOH; 1 M (a), 0.5 M (b), 0.1 M (c) and pure water (d) after 24 h cell conditioning.

the cell. A further decrease of KOH concentration to 0.1 M or pure water caused a large increase of polarisation resistance indicating a relevant role of the hydroxide ion concentration on the electrocatalytic properties.

CRediT authorship contribution statement

S. Campagna Zignani: Conceptualization, Investigation, Methodology, Visualization, Writing – original draft, Validation. **M. Lo Faro:** Investigation, Methodology, Visualization. **A. Carbone:** Investigation, Methodology. **C. Italiano:** Investigation, Methodology. **S. Trocino:** Investigation, Methodology, Data curation. **G. Monforte:** Investigation, Methodology. **A.S. Arico:** Conceptualization, Supervision, Writing –

review & editing, Funding acquisition.

Declaration of Competing Interest

The authors declare that they have no competing financial interests, there are no financial or personal relationships with other people or organizations that could have inappropriately influenced this work.

Acknowledgements

The authors acknowledge the financial support provided by the ANIONE project under the European Union's Horizon 2020 Research and Innovation Programme. This project has received funding from the Fuel Cells and Hydrogen 2 Joint Undertaking (JU) under grant agreement No 875024. The JU receives support from the European Union's Horizon 2020 Research and Innovation Programme and Italy, France, United Kingdom, Denmark, Belgium, Netherlands, Israel. The authors are also grateful to NV BEKAERT SA (Belgium) for the supply of Ni backing layers.

Supplementary materials

Supplementary material associated with this article can be found, in the online version, at doi:10.1016/j.electacta.2022.140078.

References

- [1] D. Pletcher, X. Li, Prospects for alkaline zero gap water electrolyzers for hydrogen production, *Int. J. Hydrog. Energy* 36 (2011) 15089–15104, <https://doi.org/10.1016/j.ijhydene.2011.08.080>.
- [2] K. Zeng, D. Zhang, Recent progress in alkaline water electrolysis for hydrogen production and applications, *Prog. Energy Combust. Sci.* 36 (2010) 307–326, <https://doi.org/10.1016/j.peccs.2009.11.002>.
- [3] A. Buttler, H. Spliethoff, Current status of water electrolysis for energy storage, grid balancing and sector coupling via power-to-gas and power-to-liquids: a review, *Renew. Sustain. Energy Rev.* 82 (2018) 2440–2454, <https://doi.org/10.1016/j.rser.2017.09.003>.
- [4] O. Schmidt, A. Gambhir, I. Staffell, A. Hawkes, J. Nelson, S. Few, Future cost and performance of water electrolysis: an expert elicitation study, *Int. J. Hydrogen Energy* 42 (2017) 30470–30492, <https://doi.org/10.1016/j.ijhydene.2017.10.045>.
- [5] S. Marini, P. Salvi, P. Nelli, R. Pesenti, M. Villa, M. Berrettoni, G. Zangari, Y. Kirov, Advanced alkaline water electrolysis, *Electrochim. Acta* 82 (2012) 384–391, <https://doi.org/10.1016/j.electacta.2012.05.011>.
- [6] M. Carmo, D.L. Fritz, J. Mergel, D. Stolten, A comprehensive review on PEM water electrolysis, *Int. J. Hydrogen Energy* 38 (2013) 4901–4934, <https://doi.org/10.1016/j.ijhydene.2013.01.151>.
- [7] F. Barbir, PEM electrolysis for production of hydrogen from renewable energy sources, *Solar Energy* 78 (2005) 661–669, <https://doi.org/10.1016/j.solener.2004.09.003>.
- [8] A.S. Arico, S. Siracusano, N. Briguglio, V. Baglio, A. Di Blasi, V. Antonucci, Polymer electrolyte membrane water electrolysis: status of technologies and potential applications in combination with renewable power sources, *J. Appl. Electrochem.* 43 (2013) 107–118, <https://doi.org/10.1007/s10800-012-0490-5>.
- [9] I. Sullivan, H. Zhang, C. Zhu, M. Wood, A.J. Nelson, S.E. Baker, C.M. Spadaccini, T. Van Buuren, M. Lin, E.B. Duoss, S. Liang, C. Xiang, 3D printed nickel–molybdenum-based electrocatalysts for hydrogen evolution at low overpotentials in a flow-through configuration, *ACS Appl. Mater. Interfaces* 13 (2021) 20260–20268, <https://doi.org/10.1021/acsami.1c05648>.
- [10] European Commission, Communication from the Commission to the European Parliament, the Council, the European Economic and Social Committee and the Committee of the Regions. Critical Raw Materials Resilience: charting a Path towards greater Security and Sustainability, Directorate-General for Internal Market, Industry, Entrepreneurship and SMEs, Ref. COM (2020) 474, 03/09/2020. [https://ec.europa.eu/transparency/documents-register/detail?ref=COM\(2020\)474&lang=en](https://ec.europa.eu/transparency/documents-register/detail?ref=COM(2020)474&lang=en).
- [11] J.R. Varcoe, P. Atanassov, D.R. Deke, A.M. Herring, M.A. Hickner, Paul.A. Kohl, A. R. Kucernak, W.E. Mustain, K. Nijmeijer, K. Scott, T. Xu, L. Zhuang, Anion-exchange membranes in electrochemical energy systems, *Energy Environ. Sci.* 7 (2014) 3135–3191, <https://doi.org/10.1039/C4EE01303D>.
- [12] J.E. Park, S.Y. Kang, S.-H. Oh, J.K. Kim, M.S. Lim, C.-Y. Ahn, Y.-H. Cho, Y.-E. Sung, High-performance anion-exchange membrane water electrolysis, *Electrochim. Acta* 295 (2019) 99–106, <https://doi.org/10.1016/j.electacta.2018.10.143>.
- [13] C.C. Pavel, F. Cecconi, C. Emiliani, S. Santiccioli, A. Scaffidi, S. Catanorchi, M. Comotti, Highly efficient platinum group metal free based membrane-electrode assembly for anion exchange membrane water electrolysis, *Angew. Chem. Int. Ed.* 53 (2014) 1378–1381, <https://doi.org/10.1002/anie.201308099>.

- [14] P. Fortin, T. Khoza, X. Cao, S.Y. Martinsen, A. Oyarce Barnett, S. Holdcroft, High-performance alkaline water electrolysis using Aemion™ anion exchange membranes, *J. Power Sources*. 451 (2020), 227814, <https://doi.org/10.1016/j.jpowsour.2020.227814>.
- [15] A.Y. Faid, L. Xie, A.O. Barnett, F. Seland, D. Kirk, S. Sunde, Effect of anion exchange ionomer content on electrode performance in AEM water electrolysis, *Int. J. Hydrog. Energy*. 45 (2020) 28272–28284, <https://doi.org/10.1016/j.ijhydene.2020.07.202>.
- [16] A. Carbone, S.C. Zignani, I. Gatto, S. Trocino, A.S. Aricò, Assessment of the FAA3-50 polymer electrolyte in combination with a NiMn2O4 anode catalyst for anion exchange membrane water electrolysis, *Int. J. Hydrog. Energy*. 45 (2020) 9285–9292, <https://doi.org/10.1016/j.ijhydene.2020.01.150>.
- [17] H. Ito, N. Kawaguchi, S. Satoshi, T. Munakata, Pressurized operation of anion exchange membrane water electrolysis, *Electrochim. Acta* 297 (2018), <https://doi.org/10.1016/j.electacta.2018.11.077>.
- [18] M.A. Hickner, Strategies for Developing New Anion Exchange Membranes and Electrode Ionomers, *Electrochem. Soc. Interface*. 26 (2017) 69–73, <https://doi.org/10.1149/2.f08171if>.
- [19] D. Henkensmeier, M. Najjibah, C. Harms, J. Žitka, J. Hnát, K. Bouzek, Overview: state-of-the-art commercial membranes for anion exchange membrane water electrolysis, *J. Electrochem. Energy Convers. Storage* 18 (2020), <https://doi.org/10.1115/1.4047963>.
- [20] E. Park, C. Capuano, K. Ayers, C. Bae, Chemically durable polymer electrolytes for solid-state alkaline water electrolysis, *J. Power Sources* 375 (2017), <https://doi.org/10.1016/j.jpowsour.2017.07.090>.
- [21] I. Vincent, D. Bessarabov, Low cost hydrogen production by anion exchange membrane electrolysis: a review, *Renew. Sustain. Energy Rev.* 81 (2018) 1690–1704, <https://doi.org/10.1016/j.rser.2017.05.258>.
- [22] F. Razmjooei, A. Farooqui, R. Reissner, A.S. Gago, S.A. Ansar, K.A. Friedrich, Elucidating the performance limitations of alkaline electrolyte membrane electrolysis: dominance of anion concentration in membrane electrode assembly, *ChemElectroChem* 7 (19) (2020) 3951–3960, <https://doi.org/10.1002/celec.202000605>.
- [23] D. Pletcher, X. Li, S. Wang, A comparison of cathodes for zero gap alkaline water electrolyzers for hydrogen production, 7th Petite Workshop Defect Chem, *Nat. Energy Mater.* 37 (2012) 7429–7435, <https://doi.org/10.1016/j.ijhydene.2012.02.013>, 14–17 March 2011 Storaaas Kongsberg Nor.
- [24] A.Y. Faid, A.O. Barnett, F. Seland, S. Sunde, NiCu mixed metal oxide catalyst for alkaline hydrogen evolution in anion exchange membrane water electrolysis, *Electrochim. Acta* 371 (2021), 137837, <https://doi.org/10.1016/j.electacta.2021.137837>.
- [25] M. Gong, Y. Li, H. Wang, Y. Liang, J.Z. Wu, J. Zhou, J. Wang, T. Regier, F. Wei, H. Dai, An advanced Ni–Fe layered double hydroxide electrocatalyst for water oxidation, *J. Am. Chem. Soc.* 135 (2013) 8452–8455, <https://doi.org/10.1021/ja4027715>.
- [26] Z. Lu, W. Xu, W. Zhu, Q. Yang, X. Lei, J. Liu, Y. Li, X. Sun, X. Duan, Three-dimensional NiFe layered double hydroxide film for high-efficiency oxygen evolution reaction, *Chem. Commun.* 50 (49) (2014) 6479–6482, <https://doi.org/10.1039/C4CC01625D>.
- [27] C. Kuai, Y. Zhang, D. Wu, D. Sokaras, L. Mu, S. Spence, D. Nordlund, F. Lin, X.-W. Du, Fully oxidized Ni–Fe layered double hydroxide with 100% exposed active sites for catalyzing oxygen evolution reaction, *ACS Catal.* 9 (2019) 6027–6032, <https://doi.org/10.1021/acscatal.9b01935>.
- [28] E. Fabbri, A. Haberer, K. Waltar, R. Kötz, T.J. Schmidt, Developments and perspectives of oxide-based catalysts for the oxygen evolution reaction, *Catal. Sci. Technol.* 4 (2014) 3800–3821, <https://doi.org/10.1039/C4CY00669K>.
- [29] X. Cheng, E. Fabbri, M. Nachtegaal, I.E. Castellí, M. El Kazzi, R. Haumont, N. Marzari, T.J. Schmidt, Oxygen evolution reaction on La1-xSrxCoO3 perovskites: a combined experimental and theoretical study of their structural, electronic, and electrochemical properties, *Chem. Mater.* 27 (2015) 7662–7672, <https://doi.org/10.1021/acs.chemmater.5b03138>.
- [30] J.T. Mefford, X. Rong, A.M. Abakumov, W.G. Hardin, S. Dai, A.M. Kolpak, K. P. Johnston, K.J. Stevenson, Water electrolysis on La1-xSrxCoO3-δ perovskite electrocatalysts, *Nat. Commun.* 7 (2016) 11053, <https://doi.org/10.1038/ncomms11053>.
- [31] E. Park, C. Capuano, K. Ayers, C. Bae, Chemically durable polymer electrolytes for solid-state alkaline water electrolysis, *J. Power Sources* 375 (2017), <https://doi.org/10.1016/j.jpowsour.2017.07.090>.
- [32] J. Parrondo, C.G. Arges, M. Niedzwiecki, E.B. Anderson, K.E. Ayers, V. Ramani, Degradation of anion exchange membranes used for hydrogen production by ultrapure water electrolysis, *RSC Adv.* 4 (2014) 9875–9879, <https://doi.org/10.1039/C3RA46630B>.
- [33] D. Li, A.R. Motz, C. Bae, C. Fujimoto, G. Yang, F.-Y. Zhang, K.E. Ayers, Y.S. Kim, Durability of anion exchange membrane water electrolyzers, *Energy Environ. Sci.* 14 (2021) 3393–3419, <https://doi.org/10.1039/D0EE04086J>.
- [34] A.K. Niaz, A. Akhtar, J.-Y. Park, H.-T. Lim, Effects of the operation mode on the degradation behavior of anion exchange membrane water electrolyzers, *J. Power Sources*. 481 (2021), 229093, <https://doi.org/10.1016/j.jpowsour.2020.229093>.
- [35] C. Busacca, S. Zignani, A. Blasi, O. Di Blasi, M. Lo Faro, V. Antonucci, A.S. Aricò, Electropun NiMn2O4 and NiCo2O4 spinel oxides supported on carbon nanofibers as electrocatalysts for the oxygen evolution reaction in an anion exchange membrane-based electrolysis cell, *Int. J. Hydrog. Energy*. 44 (2019) 20987–20996, <https://doi.org/10.1016/j.ijhydene.2019.02.214>.
- [36] P. Chen, X. Hu, High-Efficiency Anion Exchange Membrane water electrolysis employing non-noble metal catalysts, *Adv. Energy Mater.* 10 (2020), 2002285, <https://doi.org/10.1002/aenm.202002285>.
- [37] S.H. Ahn, B.S. Lee, I. Choi, S.J. Yoo, H.-J. Kim, E. Cho, D. Henkensmeier, S.W. Nam, S.K. Kim, J.H. Jang, Development of a membrane electrode assembly for alkaline water electrolysis by direct electrodeposition of nickel on carbon papers, *Appl. Catal. B Environ.* 154–155 (2014) 197–205, [10.1016/j.apcatb.2014.02.021](https://doi.org/10.1016/j.apcatb.2014.02.021).
- [38] V. Kuznetsov, Y. Gamburg, V.V. Zhulikov, V.M. Krutskikh, E.A. Filatova, A. Trigub, O.A. Belyakova, Electrodeposited NiMo, CoMo, ReNi, and electrodeless NiReP alloys as cathode materials for hydrogen evolution reaction, *Electrochim. Acta* 354 (2020), 136610, <https://doi.org/10.1016/j.electacta.2020.136610>.
- [39] M. Manazoglu, G. Hapçı, G. Orhan, Effect of electrolysis parameters of Ni–Mo alloy on the electrocatalytic activity for hydrogen evaluation and their stability in alkaline medium, *J. Appl. Electrochem.* 46 (2016) 191–204, <https://doi.org/10.1007/s10800-015-0908-y>.
- [40] M. Manazoglu, G. Hapçı, G. Orhan, Electrochemical Deposition and Characterization of Ni–Mo Alloys as cathode for alkaline water electrolysis, *J. Mater. Eng. Perform.* 25 (2016) 130–137, <https://doi.org/10.1007/s11665-015-1849-7>.
- [41] C. Gonsalves, A. Hegde, Electrochemical water electrolysis using electrodeposited (NiMo) coatings from a low concentration bath, *Chem. Data Collect.* 34 (2021), 100697, <https://doi.org/10.1016/j.cdc.2021.100697>.
- [42] W. Gao, W. Gou, X. Zhou, J.C. Ho, Y. Ma, Y. Qu, Amine-Modulated/Engineered Interfaces of NiMo Electrocatalysts for Improved Hydrogen Evolution Reaction in Alkaline Solutions, *ACS Appl. Mater. Interfaces*. 10 (2018) 1728–1733, <https://doi.org/10.1021/acsami.7b16125>.
- [43] A.G. Vidales, S. Omanovic, Evaluation of nickel-molybdenum-oxides as cathodes for hydrogen evolution by water electrolysis in acidic, alkaline, and neutral media, *Electrochim. Acta* 262 (2018), <https://doi.org/10.1016/j.electacta.2018.01.007>.
- [44] A.Y. Faid, A. Oyarce Barnett, F. Seland, S. Sunde, Highly Active Nickel-Based Catalyst for Hydrogen Evolution in Anion Exchange Membrane Electrolysis, *Catalysts* 8 (2018), <https://doi.org/10.3390/catal8120614>.
- [45] S. Yagi, A. Kawakami, K. Murase, Y. Awakura, Ni–Mo alloying of nickel surface by alternating pulsed electrolysis using molybdenum(VI) baths, *Electrochim. Acta* 52 (2007) 6041–6051, <https://doi.org/10.1016/j.electacta.2007.03.063>.
- [46] T. Wang, H. Wu, C. Feng, Y. Ding, H. Mei, Ni, N-codoped NiMoO4 grown on 3D nickel foam as bifunctional electrocatalysts for hydrogen production in urea-water electrolysis, *Electrochim. Acta* 391 (2021), 138931, <https://doi.org/10.1016/j.electacta.2021.138931>.
- [47] M. Schalenbach, F.D. Speck, M. Ledendecker, O. Kasian, D. Goehl, A.M. Mingers, B. Breitbach, H. Springer, S. Cherevko, K.J.J. Mayrhofer, Nickel-molybdenum alloy catalysts for the hydrogen evolution reaction: activity and stability revised, *Electrochim. Acta* 259 (2018) 1154–1161, <https://doi.org/10.1016/j.electacta.2017.11.069>.
- [48] A. Nairan, P. Zou, C. Liang, J. Liu, D. Wu, P. Liu, C. Yang, NiMo solid solution nanowire array electrodes for highly efficient hydrogen evolution reaction, *Adv. Funct. Mater.* 29 (2019), 1903747, <https://doi.org/10.1002/adfm.201903747>.
- [49] J. Lee, H. Jung, Y.S. Park, S. Woo, J. Yang, M.J. Jang, J. Jeong, N. Kwon, B. Lim, J. W. Han, S.M. Choi, High-efficiency anion-exchange membrane water electrolyzer enabled by ternary layered double hydroxide anode, *Small* 17 (2021), 2100639, <https://doi.org/10.1002/sml.202100639>.
- [50] S. Siracusanò, N. Hodnik, P. Jovanovic, F. Ruiz-Zepeda, M. Šala, V. Baglio, A. S. Aricò, New insights into the stability of a high performance nanostructured catalyst for sustainable water electrolysis, *Nano Energy* 40 (2017) 618–632, <https://doi.org/10.1016/j.nanoen.2017.09.014>.
- [51] M. Wilhelm, A. Bastos, C. Neves, R. Martins, J. Tedim, Ni-Fe layered double hydroxides for oxygen evolution reaction: impact of Ni/Fe ratio and crystallinity, *Mater. Des.* 212 (2021), 110188, <https://doi.org/10.1016/j.matdes.2021.110188>.
- [52] G. Dong, F. Xie, F. Kou, T. Chen, F. Wang, Y. Zhou, K. Wu, S. Du, M. Fang, J.C. Ho, NiFe-layered double hydroxide arrays for oxygen evolution reaction in fresh water and seawater, *Mater. Today Energy* 22 (2021), 100883, <https://doi.org/10.1016/j.mtener.2021.100883>.
- [53] Q. Han, Y. Luo, J. Li, X. Du, S. Sun, Y. Wang, G. Liu, Z. Chen, Efficient NiFe-based oxygen evolution electrocatalysts and origin of their distinct activity, *Appl. Catal. B Environ.* 304 (2022), 120937, <https://doi.org/10.1016/j.apcatb.2021.120937>.
- [54] J. Hu, Y.Q. Liang, S.L. Wu, Z.Y. Li, C.S. Shi, S.Y. Luo, H.J. Sun, S.L. Zhu, Z.D. Cui, Hierarchical nickel-iron layered double hydroxide composite electrocatalyst for efficient oxygen evolution reaction, *Mater. Today Nano* 17 (2022), 100150, <https://doi.org/10.1016/j.mtnano.2021.100150>.
- [55] H. Xu, W.-D. Zhang, J. Liu, Y. Yao, X. Yan, Z.-G. Gu, Intercalation-induced partial exfoliation of NiFe LDHs with abundant active edge sites for highly enhanced oxygen evolution reaction, *J. Colloid Interface Sci.* 607 (2022) 1353–1361, <https://doi.org/10.1016/j.jcis.2021.09.105>.
- [56] J.L. Xu, L.L. Li, J. Tang, L. Dai, X.B. Li, Z.G. Ye, J.M. Luo, Powder metallurgy synthesis of porous NiMo alloys as efficient electrocatalysts to enhance the hydrogen evolution reaction, *J. Alloys Compd.* 865 (2021), 158901, <https://doi.org/10.1016/j.jallcom.2021.158901>.
- [57] C. González-Buch, I. Herraiz-Cardona, E. Ortega, J. García-Antón, V. Pérez-Herranz, Study of the catalytic activity of 3D macroporous Ni and NiMo cathodes for hydrogen production by alkaline water electrolysis, *J. Appl. Electrochem.* 46 (2016), <https://doi.org/10.1007/s10800-016-0970-0>.
- [58] A.Y. Faid, A.O. Barnett, F. Seland, S. Sunde, Tuning Ni–MoO2 Catalyst–Ionomer and Electrolyte Interaction for Water Electrolyzers with Anion Exchange Membranes, *ACS Appl. Energy Mater.* 4 (2021) 3327–3340, <https://doi.org/10.1021/acsaem.0c03072>.
- [59] V.V. Kuznetsov, Y.D. Gamburg, V.V. Zhulikov, R.S. Batalov, E.A. Filatova, Re–Ni cathodes obtained by electrodeposition as a promising electrode material for hydrogen evolution reaction in alkaline solutions, *Electrochim. Acta* (2019).

- [60] S. Campagna Zignani, M. Lo Faro, S. Trocino, A.S. Aricò, Investigation of NiFe-based catalysts for oxygen evolution in anion-exchange membrane electrolysis, *Energies* (2020) 13, <https://doi.org/10.3390/en13071720>.
- [61] R. Zhang, P.A. Russo, A.G. Buzanich, T. Jeon, N. Pinna, Hybrid organic-inorganic transition-metal phosphonates as precursors for water oxidation electrocatalysts, *Adv. Funct. Mater.* 27 (2017), 1703158, <https://doi.org/10.1002/adfm.201703158>.
- [62] J.R. McKone, B.F. Sadtler, C.A. Werlang, N.S. Lewis, H.B. Gray, Ni-Mo nanopowders for efficient electrochemical hydrogen evolution, *ACS Catal.* 3 (2013) 166–169, <https://doi.org/10.1021/cs300691m>.
- [63] H.L.S. Santos, P.G. Corradini, M. Medina, J.A. Dias, L.H. Mascaro, NiMo-NiCu inexpensive composite with high activity for hydrogen evolution reaction, *ACS Appl. Mater. Interfaces.* 12 (2020) 17492–17501, <https://doi.org/10.1021/acscami.0c00262>.
- [64] A. Patterson, The Scherrer Formula for X-Ray Particle size determination, *Phys. Rev.* 56 (10) (1939) 978–982, <https://doi.org/10.1103/PhysRev.56.978>.
- [65] E.S. Davydova, F.D. Speck, M.T.Y. Paul, D.R. Dekel, S. Cherevko, Stability limits of ni-based hydrogen oxidation electrocatalysts for anion exchange membrane fuel cells, *ACS Catal.* 9 (8) (2019) 6837–6845, <https://doi.org/10.1021/acscatal.9b01582>.
- [66] J.F. Moulder, W.F. Stickle, P.E. Sobol, K.D. Bomben, *Handbook of X-Ray Photoelectron Spectroscopy*, Physical Electronics, Inc., Eden Prairie, MN, 1995.
- [67] P. Chagas, A.C. da Silva, E.C. Passamani, J.D. Ardisson, L.C. Alves de Oliveira, J. D. Fabris, R.M. Paniago, D.S. Monteiro, M.C. Pereira, δ -FeOOH: a superparamagnetic material for controlled heat release under AC magnetic field, *J. Nanoparticle Res. J. Nanopart. Res.* 15 (2013) 1544–1551, <https://doi.org/10.1007/s11051-013-1544-2>.
- [68] A. Davidson, J.F. Tempere, M. Che, H. Roulet, G. Dufour, Spectroscopic studies of Nickel(II) and Nickel(III) species generated upon thermal treatments of nickel/ceria-supported materials, *J. Phys. Chem.* 100 (1996) 4919, <https://doi.org/10.1021/jp952268w>. –492.
- [69] V.M. Nikolic, S. Lj. Maslovara, G.S. Tasic, T.P. Brdaric, P.Z. Lausevic, B.B. Radak, M.P. Marceta Kaninski, Kinetics of hydrogen evolution reaction in alkaline electrolysis on a Ni cathode in the presence of Ni-Co-Mo based ionic activators, *Appl. Catal. B: Environ.* 179 (2015) 88–94, <https://doi.org/10.1016/j.apcatb.2015.05.012>.
- [70] T. Shinagawa, A. Garcia-Esparza, K. Takanabe, Insight on Tafel slopes from a microkinetic analysis of aqueous electrocatalysis for energy conversion, *Sci. Rep.* 5 (2015) 13801–13821, <https://doi.org/10.1038/srep13801>.
- [71] L. Negahdar, F. Zeng, S. Palkovits, C. Broicher, R. Palkovits, Mechanistic aspects of the electrocatalytic oxygen evolution reaction over Ni Co oxide, *ChemElectroChem* 6 (2019) 5588–5595, [10.1002/celec.201901265](https://doi.org/10.1002/celec.201901265).
- [72] J. Park, J.H. Jang, A. Lee, S. Kim, S. Lee, S.J. Yoo, J. Lee, Effect of support for non-noble NiMo electrocatalyst in alkaline hydrogen oxidation, *Adv. Sustain. Syst.* (2021), 2100226, <https://doi.org/10.1002/adsu.202100226> n/a.
- [73] F. Razmjooei, T. Morawietz, E. Taghizadeh, E. Hadjixenophontos, L. Mues, M. Gerle, B.D. Wood C. Harms, A.S. Gago, S.A. Ansar, K.A. Friedrich, Increasing the performance of an anion-exchange membrane electrolyzer operating in pure water with a nickel-based microporous layer, *Joule* 5 (7) (2021) 1776–1799, <https://doi.org/10.1016/j.joule.2021.05.006>.
- [74] G.A. Lindquist, S.Z. Oener, Raina Krivina, Andrew R. Motz, Alex Keane, Christopher Capuano, K.E. Ayers, S.W. Boettcher, Performance and durability of pure-water-fed anion exchange membrane electrolyzers using baseline materials and operation, *ACS Appl. Mater. Interfaces* 13 (2021) 51917–51924, <https://doi.org/10.1021/acscami.1c06053>.